

ALMA MATER STUDIORUM · UNIVERSITÀ DI
BOLOGNA

Scuola di Scienze
Corso di Laurea Magistrale in Fisica

Novel materials for direct X-ray detectors
based on semiconducting organic polymers

Relatore:
Prof.ssa Beatrice Fraboni

Presentata da:
Marco Carroli

Correlatore:
Dott. Tobias Cramer

Sessione II
Anno Accademico 2014/2015

Abstract

Conventional inorganic materials for x-ray radiation sensors suffer from several drawbacks, including their inability to cover large curved areas, mechanical stiffness, lack of tissue-equivalence and toxicity. Semiconducting organic polymers represent an alternative and have been employed as direct photoconversion material in organic diodes. In contrast to inorganic detector materials, polymers allow low-cost and large area fabrication by solvent based methods. In addition their processing is compliant with flexible low-temperature substrates. Flexible and large-area detectors are needed for dosimetry in medical radiotherapy and security applications. The objective of my thesis is to achieve optimized organic polymer diodes for flexible, direct x-ray detectors. To this end polymer diodes based on two different semiconducting polymers, polyvinylcarbazole (PVK) and poly(9,9-dioctylfluorene) (PFO) have been fabricated. The diodes show state-of-the-art rectifying behaviour and hole transport mobilities comparable to reference materials. In order to improve the X-ray stopping power, high-Z nanoparticle Bi₂O₃ or WO₃ were added to realize a polymer-nanoparticle composite with optimized properties. X-ray detector characterization resulted in sensitivities of up to 14 $\mu\text{C}/\text{Gy}/\text{cm}^2$ for PVK when diodes were operated in reverse. Addition of nanoparticles could further improve the performance and a maximum sensitivity of 19 $\mu\text{C}/\text{Gy}/\text{cm}^2$ was obtained for the PFO diodes. Compared to the pure PFO diode this corresponds to a five-fold increase and thus highlights the potentiality of nanoparticles for polymer detector design. Interestingly the pure polymer diodes showed an order of magnitude increase in sensitivity when operated in forward regime. The increase was attributed to a different detection mechanism based on the modulation of the diodes conductivity.

Contents

Introduction	1
1 X-ray detectors: an overview on direct detection	7
1.1 Semiconductors X-ray detectors	9
1.1.1 The ionizing interaction in semiconductors	12
1.2 Semiconducting conjugated polymers for radiation detection .	16
1.3 Schottky and ohmic contacts	17
1.4 Current-voltage characteristics	24
2 Semiconducting polymers	29
2.1 Introduction	29
2.2 Structural Characteristics	30
2.2.1 Conduction mechanisms	33
2.3 Blend of Nanoparticles in Polymers	37
3 Materials and Method	41
3.1 Introduction	41
3.2 Materials	41
3.3 Diode fabrication process	43
3.4 Diode Fabrication Techniques	46
3.4.1 Thermal evaporation	46
3.4.2 Spin-coating	47
3.5 Electrical Characterization	49
3.6 X-ray characterization of fabricated diodes	50
3.7 Fabrication of Nanoparticle Polymer Diodes	52
3.8 Structural Characterization	53

3.8.1	Atomic Force Microscopy	54
3.8.2	SEM	60
3.8.3	TEM	61
4	Results	63
4.1	Pristine PVK and PFO diodes	63
4.1.1	Electrical characterization	64
4.1.2	X-ray detector properties	70
4.1.3	Discussion and conclusion	73
4.2	NP-polymer blend diodes	76
4.2.1	Morphological characterization	77
4.2.2	Electrical characterization	82
4.2.3	X-ray detector properties	84
4.2.4	Discussion and conclusion	86
5	Conclusions	89
	Bibliography	99

Introduction

A new generation of radiation detectors is required to improve on existing devices. Radiation detectors are needed for several advanced applications such as particle physics experiments [1], dosimetry in medical radiotherapy [2], and for security purposes [3]. Each of these applications has specific material requirements that are driving further development. Methods for the indirect detection of radiation rely on a secondary transduction method, such as the modulation or quenching of optical properties [4] or scintillation in combination with a phosphor screen [5]. Of more practical use, and the topic of this present work, is the direct detection of radiation. In this case, the radiation exposure induces a photo current that can be correlated with the radiation dose in a quantitative way. Solid-state radiation detectors for the direct detection of radiation have conventionally been based on inorganic materials. In detectors for synchrotron or linear accelerators used by particle physicists, large areas in curved geometries are needed. However, large-area, high quality inorganic crystals are expensive and difficult to manufacture. The detector is limited to sizes up to twelve inches for silicon, as defined by the requirements of the electronics industry, but much smaller dimensions for other, more exotic crystalline materials. In medical radiation dosimetry and radiation protection applications, on the other hand, there is a need for detectors that have tissue equivalence for dose estimations (dosimetry) to the human body, and which minimise beam perturbations [6]. This requirement means that the dosimeters must be comprised of the elements of human tissue, e.g. C, H, and O. Inorganic semiconductors being applied in dosimeters, such as CdTe [7] and CdZnTe, are comprised of heavy elements and hence are not tissue equivalent. Dosimeters that are in regular contact with humans must be made from materials that are not toxic. Hence, Cd-containing

materials are excluded from such applications. Furthermore, the high cost of single-crystal inorganic semiconductors is also driving the development of new dosimeter materials.

There are specific property performance requirements for detectors or dosimeters that must be met by any new material. Silicon, which can be used a standard to judge new materials, has a radiation length of 9.4 cm [8] and has a high mobility (450 cm²/Vs and 1400 cm²/Vs for holes and electrons, respectively) [9]. The leakage current measured from a Si pin diode in the reverse bias operation is extremely low (less than 1 nA). Ideally, the new detector material should have a low dark current (< 1 nA), good rectification behavior, high charge-carrier mobility, and outstanding operational stability. Clearly, the demands for detector materials are great, yet conjugated polymers can potentially meet them. Conjugated polymers are those polymers with an extended π -bonding system. The research in this particular field received little attention from the community before 1970 due to unprecedented physical properties, such as poor electrical and optical properties. However, some research groups reported an unusually high electrical conductivity in some conjugated polymers. The mystery of high conductivity in these polymers remained unsolved until 1977 when Shirakawa et al. first discovered that the conductivity of poly(acetylene) increased due to a redox reaction when exposed to bromine or iodine vapour. Since then semiconducting polymers have drawn great attention from researchers around the world from both fundamental and technological points of view. Semiconducting polymers have been in the heart of interdisciplinary research and development, ranging from physics, materials science, chemistry, engineering, and technology. High quality organic electronic devices have been achieved through the improvement of the quality of π -conjugated polymers. The fabrications of organic devices, including field effect transistors [10], light emitting diodes, photovoltaic cells [11], and sensors [12], have employed organic materials as an active component in the device. These devices share one common feature, their efficiency depends tremendously on the ability of the conjugated polymer to transport charge carriers. The charge carriers can either be generated within the polymer layer (solar cells or sensors) or injected into the polymer layer from the metal contact (LED or FETS). Despite vibrant activity in

the organic electronics field, the use of conjugated polymers for the detection of ionizing radiation has received comparatively little attention from the community.

Semiconducting polymers have been previously used to detect a variety of radiations. The detection of charged particles has been achieved by using conjugated polymers, such as poly(phenylene vinylene) (PPV) and its derivatives. In this case, the optical properties of the material are modulated or quenched after exposure to protons [13] or gamma radiation. Organic photodiodes, used as scintillation detectors when combined with phosphor screens, have demonstrated a good sensitivity and stability upon X-ray irradiation [14]. However, these examples can be classified as using indirect detection methods, which are based on a secondary transduction method, such as the optical monitoring of turbidity or scintillation. Of more practical use are detectors in which the radiation exposure directly triggers a change in the electrical conduction in the detector (direct detection). Yoshino et al were the first group to establish the possibility of using conjugated polymers for radiation detection by studying the effects of electron irradiation on the conductivity of Iodine-doped polyacetylene (PA) at room temperature [15]. Recently, the group at the University of Surrey has recently shown that direct X-ray induced photocurrent can be observed in metal/polymer/metal diode structures [16] indicating the feasibility of using conjugated polymers in direct real-time radiation detection applications. However, the performance stability, measurement repeatability, and signal quality of such organic detectors upon exposure to X-rays have not previously been reported. The question remains whether organic material-based detectors are suitable for employment in solid-state radiation detection applications. Current radiation dosimetry systems, based on scintillators or semiconductors, typically use inorganic materials as the active counterpart [17]. Such materials can be fragile and difficult to machine, and hence are undesirable for large area, curved surface, thin film detector production. The use of semiconducting polymers in electronic devices offers many advantages over their conventional inorganic counterparts. Polymers have a mechanical flexibility and light weight which makes bending or coating over curved surfaces possible. The cost of polymers is relatively low, and also materials are now commercially available as the de-

mand is high. Polymers are very easy to fabricate since no clean room, high temperature or low pressure conditions are required in the preparation processes. Typical conjugated polymers have chemical side groups which enable them to be easily dissolved in organic solvents. Therefore, the fabrication of polymer films can be performed over large area substrates using low-cost, wet processing techniques, such as spin-casting [18], dip-coating [19], spray-casting [20] and inkjet printing [21]. Conjugated polymers, however, have suffered from a relatively low carrier mobility and poor stability under ambient conditions compared to inorganic materials. Due to their low atomic number, conjugated polymers provide a low stopping power for ionizing particles compared to the conventional material for detectors, such as CdTe. These are the major drawbacks for semiconducting polymers to match inorganic semiconductor-based devices in radiation detector applications. For charge-based ionizing radiation detectors and dosimeters, certain requirements need to be met in order to have a usable device, such as low leakage current at high electric field strengths, chemical and electronic stability, high carrier mobility and high quantum efficiency upon exposure to an ionizing source. Low leakage current at high field strengths can be realised by the formation of a Schottky contact at the polymer/metal interface. The sensitivity upon X-ray exposure can be significantly improved by having a large capture volume of an active material. This can be achieved by either increasing the thickness of the polymer or the active area of the device. In this work, Polyvinylcarbazole (PVK) and poly(9,9-dioctylfluorene) (PFO) are selected for active layer of the devices due to a number of reasons. Both polymers are operationally and environmentally stable and both have been already used as a hole transport layer [22] in organic light emitting diode (OLED). Furthermore, these polymers are much cheaper (ref:Sigma-Aldrich) than poly(triarylamine) (PTAA) used by the Sellin group.

In this project, the main objective is to explore the feasibility of using a thick layer of PVK (PFO) as a charge-sensitive, direct-detection radiation dosimeter. The thesis begins with a review on x-ray detectors, focusing on the direct X-ray detection and on the X-ray interaction with matter in Chapter 1. At the end of the Chapter 1, the organic X-ray detectors are described. Chapter 2 introduces to the science of organic semiconductors,

including the conduction mechanisms, electronic structure, charge transport properties and device applications. Chapter 3 explains the materials used in the experiments and the device fabrication processes. The physical background, as well as the details of the scientific apparatus for every experimental technique employed in the project, is also provided in this chapter. The fabrication of prototype organic semiconductor dosimeters using thick PVK or PFO films is presented. Here, the polymer films were blended with different concentrations of high atomic number (Z) nanoparticles, WO_3 and Bi_2O_3 , to enhance the X-ray stopping power of the devices. In Chapter 4, the structural and conductive properties of PVK (PFO)-based diode are presented. The hole transport through the polymers and the diode conductivity are examined by comparing the results obtained from PVK and PFO layer with different thickness. The x-ray sensitivity of the devices is assessed in different operative regime of diode (forward and reverse), as well as the type of detection. In particular, an elementary explanation of the X-ray photodetection regimes is introduced. The effects of NPs on the diode performance as detectors are evaluated by the comparison between the pristine and NP-diode. Finally, Chapter 5 summarizes the findings in this study and potential outlook to pursue in future investigation.

Chapter 1

X-ray detectors: an overview on direct detection

Since 1950, we have witnessed the development of a range of radiation detectors exploiting the properties of semiconductor materials. The steady growth of these devices is primarily due to the numerous application fields: medical imaging and diagnostics, industrial and civil security, astrophysics. The materials employed in the past 60 years fall mainly into two categories sketched in the figure 1.1: semiconductors and scintillators. In both cases, X-ray irradiation first produces primary excitations and ionizations (ions and electrons) in the time range of 10^{-15} - 10^{-13} s. The generated electrons (primary electrons) with high kinetic energy interact within the volume of the detection material and produce a majority of secondary excitations (electron-hole pairs), within a picosecond. Both primary and secondary excitations are electron-hole pairs, referred to as “excitons”. These excitons are detected following different pathways in semiconductor detectors and scintillators. In a semiconductor detector, an electric field is applied to disassociate the electron-hole pairs and sweep the electrons and holes to the positive and negative electrodes, respectively. The resulting photocurrent is recorded to analyze the energy of the incident high-energy radiation particles. In a scintillator, the excitons transfer their energy to luminescent centers (fluors) that are intentionally introduced. The fluors release the energy radiatively, via a fluorescence or phosphorescence decay pathway. The resulting photons, typi-

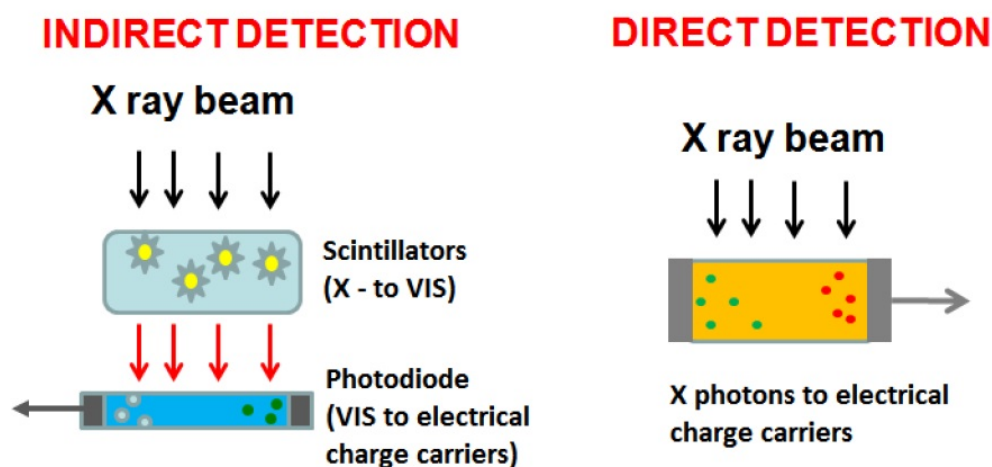


Figure 1.1: Schematic representation of indirect detection (left) and direct detection (right).

cally in the visible wavelength range, escape the scintillator and are collected by a coupled photo-multiplier tube (PMT) or a photodetector to obtain information about the incident particles. The material requirements for the two different detection mechanisms share some similarities: high stopping power (absorption efficiency) of incident radiation, high purity to lessen exciton trapping, uniformity for minimal scattering and good transparency, as well as the ability to grow material into large size. For semiconductors, a high and balanced carrier mobility and low intrinsic carrier density are essential to obtain high sensitivity and low background current. On the other hand, scintillators must have an efficient cascade energy transition series to achieve high light yield. [23]

Among the novel materials which could push the boundaries of radiation detection further, organic p-conjugated small molecules and polymers are interesting emerging candidates, thanks to their potential to realize large area and flexible optoelectronic devices [24] by cost effective printing methods, which is due to their processing from solution at room temperature. Conjugated polymers, which were first suggested for radiation detection in the early 1980s, nowadays could potentially lead to a new class of radiation detection materials outside the scope of traditional detectors.

1.1 Semiconductors X-ray detectors

A lot of radiation detection applications employ the advantages offered by direct detection. The direct conversion of ionizing radiation into an electrical signal within the same device is a more effective process than the indirect one, since it improves the signal-to-noise ratio and it reduces the device response time. One of the major limitations of scintillation counters is their relatively poor energy resolution. The chain of events that must take place in converting the incident radiation energy to light and the subsequent generation of an electrical signal involves many inefficient steps. Therefore, the energy required to produce one information carrier (a photoelectron) is of the order of 100 eV or more, and the number of carriers created in a typical radiation interaction is usually no more than a few thousand. The use of semiconductor materials as direct radiation detectors can result in a much larger number of carriers for a given incident radiation event. Consequently, the best energy resolution from radiation spectrometers in routine use is achieved using semiconductor detectors. The fundamental information carriers are electron-hole pairs created along the path taken by the primary radiation or secondary particle through the detector. Their motion in an applied electric field generates the basic electrical signal from the detector. Devices employing semiconductors as the basic detection medium became practically available in the early 1960s. Early versions were called crystal counters, but modern detectors are referred to as semiconductor diode detectors. In addition to superior energy resolution, semiconductor detectors can also have a number of other desirable features. Among these are compact size, relatively fast timing characteristics, and an effective thickness that can be varied to match the requirements of the application. Drawbacks may include the limitation to small sizes and the relatively high susceptibility of these devices to performance degradation from radiation-induced damage. The ability to detect high energy radiation such as X-rays, gamma-rays, and other uncharged and charged particles with solid-state semiconductor detectors has improved dramatically in the last 20 years thanks to two main factors: (i) the enormous advances in semiconductor science and technology, and (ii) the strong and increasing demand for high-performing solid-state radiation detectors. High purity silicon and ger-

ermanium were the first materials to be used as solidstate detectors, and are still widely employed thanks to their extremely good energy resolution (below 0.2%) which, however, can only be achieved at cryogenic temperatures. This prompted the development of novel compound semiconductors such as CdTe, SiC and CdZnTe which can offer excellent performance at room temperature, superior in a few aspects to Ge. Nonetheless, the difficulty to grow large-size, high-quality crystals of these II– VI compound materials at a low cost is limiting their application in very high-tech and specific detectors, e.g. in satellites and as pioneering medical diagnostic tools. A non-negligible further drawback of these materials is their limited availability, often their toxicity. These limitations have prompted the need to find alternative novel semiconducting materials (see section ??).

Photoconductor Material Properties The characteristics required in order to achieve a photoconductor material are several:

- *Quantum Efficiency Q.E.* Also called Attenuated fraction is defined as:

$$Q.E. = 1 - e^{-L/\delta} \quad (1.1)$$

where δ is the attenuation depth and must be substantially less than the photoconductor layer thickness L . $\delta = \delta(E_{ph}, Z, \rho)$ is a function of photon energy, atomic number and density, and can be correlated to the mass attenuation coefficient. High-Z element are suitable photoconductors, especially for high energies application.

- *Dark Current.* The dark current of the photoconductor under a bias voltage should be small. Two factors affect the dark current flowing in a material: the injection of carriers from the contact and the thermal generation of carriers. This implies that small dark current needs blocking contacts and a wide semiconductor bandgap to reduce thermal carrier generation. A generally accepted dark current should be below 1 nA/cm².
- *Charge Collection Efficiency η_{CC} .* The photogenerated charges could be lost due to recombination or trapping during the charge transport

from the collection at the electrodes. The mean distance that a carrier can go through without occurring in recombination or trapping is called drift length and it is defined as $\mu\tau F$, where F is the electric field, μ is the carrier mobility and τ is the mean lifetime of carriers. In order to reduce loss and maximize η_{CCE} , the condition $\mu\tau F \gg L$ should be satisfied for both electrons and holes (L is the layer thickness).

- *Radiation Hardness.* A detector is exposed to high x-ray doses over time, so the damage and structural changes due to irradiation have to be taken into account. The primary effect is the generation of trapping sites that modify $\mu\tau$ of the carriers and polarize the sample affecting the charge collection efficiency.
- *X-ray Sensitivity.* The detection process involves three stages: X-ray absorption (Q.E.), charge carriers generation and collection. The x-ray sensitivity of a photoconductor can be defined as the charge collected per unit of incident radiation per unit area ($C \cdot cm^{-2} \cdot Gy^{-1}$):

$$S = \frac{\text{charge collected}}{\text{incident radiation} \cdot \text{area}} \quad (1.2)$$

$$S = \left(\frac{5,45 \cdot 10^{13} e}{(\alpha_{en}/\alpha) E_{ph}} \right) \cdot Q.E. \cdot \left(\frac{(\alpha_{en}/\rho)_{air}}{\epsilon} \right) \quad (1.3)$$

where ϵ is the amount of energy to create a free electron-hole pair. The eq.1.3 summarizes well the entire detection process: the first term is the photon frequency per unit of roentgen, the second is the absorbed fraction in terms of quantum efficiency, the third is the number of electron-hole pairs generated and the last is the charge collection efficiency. The sensitivity has a strong dependence on the photodetector thickness L , since the x-ray absorption enhances as L increases, but η_{CC} decreases with L at the same electric field: therefore there is an optimum thickness value beyond which the sensitivity decreases [25]. Therefore, from experimental point of view, plotting the signal current, i.e. the charge collected, in function of the incident radiation dose rate is possible to estimate the X-ray detector sensitivity as the slope of the

linear fit of the plot.

1.1.1 The ionizing interaction in semiconductors

The interaction of radiation with semiconductor materials causes the creation of electron–hole pairs that can be detected as electric signals. The photons have first to undergo an interaction with a target electron (photo or Compton effect) or with the semiconductor nucleus (e.g. pair conversion of photons). In any case, part of the energy absorbed in the semiconductor will be converted into ionization (the creation of electron–hole pairs), the rest into phonons (lattice vibrations), which means finally into thermal energy. In the photoelectric absorption process, a photon undergoes an interaction with an absorber atom in which the photon completely disappears. In its place, an energetic photoelectron is ejected by the atom from one of its bound shells. The interaction is with the atom as a whole and cannot take place with free electrons. For gamma rays of sufficient energy, the most probable origin of the photoelectron is the most tightly bound or K shell of the atom. The photoelectron appears with an energy given by $K = h\nu - E_b$, where E_b is the binding energy of the shell and ν the frequency of the photon. The emitted electron leaves a vacancy site in the inner shells of the atom that is quickly filled through a capture of an electron from outer shells. This transition generates the emission of characteristic x-ray photons of K, L or M shells. In some cases the relaxation takes place through the emission of an Auger electron that may substitute the characteristic radiation. Furthermore, the emitted photoelectrons, the characteristic radiation and the Auger electrons may be reabsorbed, thus a complex cascade sequence of electron transitions and x-ray emissions. As the photoelectric effect, also the Compton (or Incoherent) scattering takes place between a photon and an electron in the absorbing materials. In this process the photon is deflected and transfers a portion of its energy. The Compton scattering probability increase with the number of electrons of the target material, and is typically dominant at photon energies of MeV. The pair production process arises at higher energy, when the photon energy exceeds twice the rest-mass of an electron (1.02 MeV). In this process, the photon interacts with coulomb field

of a nucleus, having enough energy to create an electron-positron pair. In the medium the pair is slowed down and the positron then annihilates with the emission of two photons as secondary products of the interaction. Even if the process is energetically possible at 1.02 MeV, its probability is still very low and rises only at very high energies. The photoelectric absorption is the dominant process at low radiation energies, and plays the main role in the absorption mechanism that occur in x-ray detectors for medical, diagnostic or imaging applications. In this process, the fraction of energy converted into electron-hole pair creation is a property of the detector material. A photoconductor with high intrinsic x-ray sensitivity must be able to generate as many collectable (free) electron hole pairs as possible per unit of absorbed radiation. The amount of radiation energy required, denoted as ϵ , to create a single free electron and hole pair is called the electron-hole pair creation energy or the ionization energy; and it should be as low as possible because the free (or collectable) charge, ΔQ , generated from an incident and absorbed radiation of energy E is simply eE/ϵ , where e is the elementary charge. For many material systems ϵ is proportional to the bandgap E_g .

Very important aspects of the detector material in spectroscopic applications are the penetration depth of charged particles and the absorption length of photons. A very small absorption length will result in a high probability of generating the signal close to the surface, where signal charge may only be partially collected because of surface treatment (e.g. doping), coverage with insensitive material (e.g. a naturally or artificially grown insulation layer) or deterioration in the semiconductor properties, which usually appears close to the surface due to distortion of the lattice. A very large absorption length leads to inefficiencies as radiation may traverse the detector without interaction.

Attenuation coefficients If we again picture a transmission experiment as in Fig. 1.2, where monoenergetic X-rays are collimated into a narrow beam and allowed to strike a detector after passing through an absorber of variable thickness, the result should be simple exponential attenuation of the X-rays as also shown in Fig. 1.2. Each of the interaction processes removes the X-ray photon from the beam either by absorption or by scattering away from the

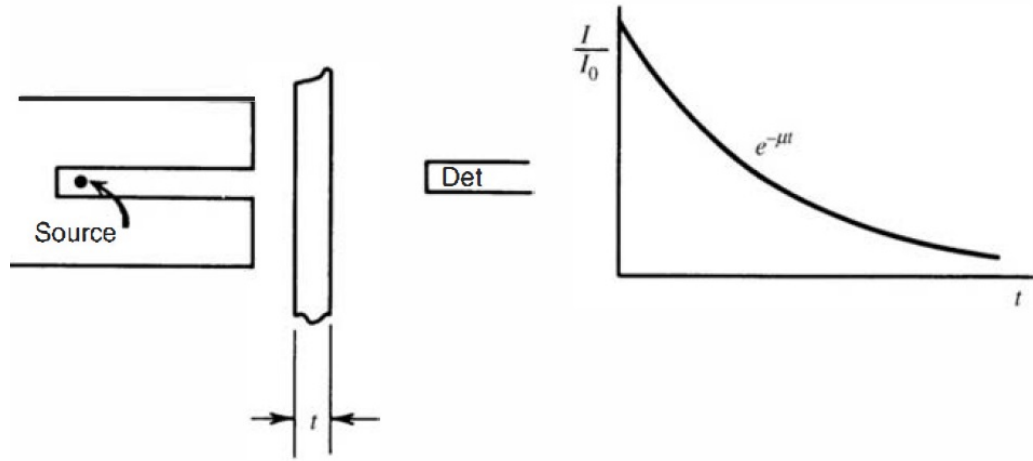


Figure 1.2: (Left) Schematic set up for transmission experiment. (Right) Exponential transmission curve.

detector direction and can be characterized by a fixed probability of occurrence per unit path length in the absorber. The sum of these probabilities is simply the probability per unit path length that the X-ray photon is removed from the beam:

$$\mu = \tau(\text{photoelectric}) + er(\text{Compton}) + K(\text{pair}) \quad (1.4)$$

and is called the linear attenuation coefficient. The number of transmitted photons I is then given in terms of the number without an absorber I_0 as

$$I = I_0 e^{-\mu t} \quad (1.5)$$

The X-ray photons can also be characterized by their mean free path λ , defined as the average distance traveled in the absorber before an interaction takes place. Its value can be obtained from

$$\lambda = \frac{\int_0^{\infty} x e^{-\mu x} dx}{\int_0^{\infty} e^{-\mu x} dx} = \frac{1}{\mu} \quad (1.6)$$

and is simply the reciprocal of the linear attenuation coefficient. Typical values of λ . range from a few mm to tens of cm in solids for common X-ray

energies. Use of the linear attenuation coefficient is limited by the fact that it varies with the density of the absorber, even though the absorber material is the same. Therefore, the mass attenuation coefficient is much more widely used and is defined as $\frac{\mu}{\rho}$, where ρ represents the density of the medium. For a given X-ray energy, the mass attenuation coefficient does not change with the physical state of a given absorber. For example, it is the same for water whether present in liquid or vapor form.

KERMA and Absorbed dose Photons interact with matter through two stages: (i) energy is transferred to charged particles and (ii) charged particles transfer energy directly through excitations and ionizations. The first interaction can be described with Kinetic Energy Released per unit Mass (KERMA) in a medium, and is defined as:

$$\kappa = \frac{dE_{tr}}{dm} \quad (1.7)$$

where E_{tr} stands for the kinetic energy transferred to the medium. The second stage of energy transfer in a medium is described with the absorbed dose, which is the energy absorbed from any type of radiation per unit mass of the absorber. The unit in SI is joule per kilogram (J/kg) and it is named as Gray(Gy). Sometimes it may be reported as the old CGS definition of erg/gram named rad. Thus $1 \text{ Gy} = 1 \text{ J/kg} = 100 \text{ rad}$. An exposure of 1 R corresponds to an absorbed dose in air of $8,7 \cdot 10^{-3} \text{ Gy}$. The energy transfer to the charge particles (Kerma) does not take place at the same location of the energy absorption, because a charge particle moves into the medium before being absorbed. However in a thick medium, if the condition of electronic equilibrium has been reached, $E_{tr} = E_{ab}$, thus the KERMA can be considered equal to Absorbed dose. Electronic equilibrium is reached when, in each moment, in every volume of the medium an equal number of particles are stopped and set in motion. The mathematical expression for the absorbed dose is reported in the following equation:

$$D = \frac{dE_{ab}}{dm}. \quad (1.8)$$

1.2 Semiconducting conjugated polymers for radiation detection

In the past two decades, conjugated polymers have been employed in the fabrication of light-emitting diodes, field-effect transistors, photovoltaic devices, and superconductors. The advantages of polymers over conventional inorganic semiconductors are their relatively low cost, suitability for both large areas and nanoscale applications, mechanical flexibility, and most importantly, the potential for printable electronic circuits for integrated plastic electronics. The use of conjugated polymers for ionizing radiation detection is likewise expected to offer several advantages in comparison to silicon, which is the most commonly used semiconductor for high fluence x-ray detection, e.g., at synchrotron sources or for medical dosimetry. Unlike silicon, polymers can be coated over large areas and onto curved surfaces through deposition from solutions in volatile solvents, such as in dip coating, spin casting, and ink-jet printing. Furthermore, polymers have a low average atomic number, which makes them equivalent to human tissue when used in x-ray dosimetry in clinical applications. Despite these potential advantages, very little attention has been paid to the application of polymers in direct charge-based radiation detection, as opposed to passive thermoluminescent or optical dosimeters. Early studies in the 1950s of insulating polymers, such as polymethyl methacrylate and polyethylene, as tissue-equivalent x-ray dosimetry detectors concluded that the combination of very low mobilities and short carrier lifetimes severely limited their x-ray sensitivity. More recently, alpha particle sensitivity has been demonstrated from polyacetylene sheets which showed drift mobilities of 10^{-4} and 10^{-3} $\text{cm}^2/\text{V s}$ for electrons and holes, respectively. With such a relatively low mobility, when such a material is used in a detector, it must be kept rather thin in order to extract a useful current. However, there is a trade-off against the requirement to use a thicker detection layer to achieve a sufficient interaction volume. For x-ray dosimetry use a polymer-based detector should have a sensitivity comparable to that of silicon, which is typically of the order of 300 nC/mGy/cm^3 .

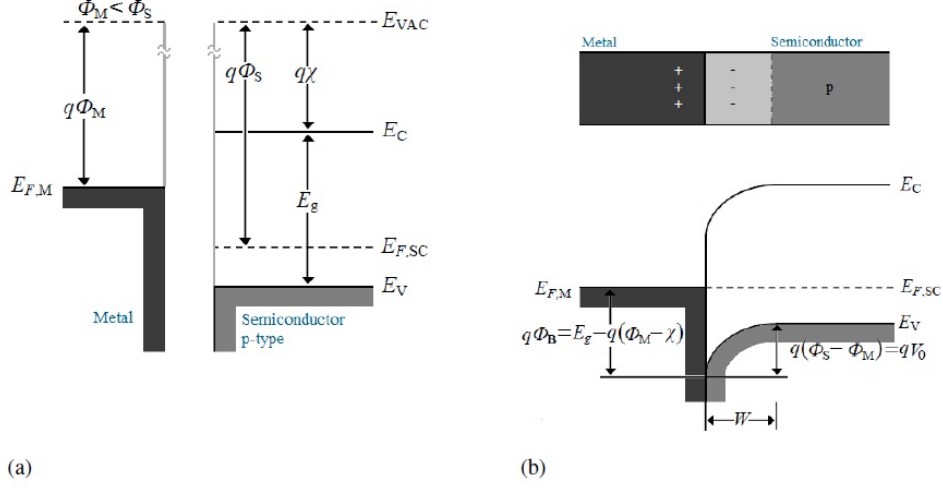


Figure 1.3: Schottky barrier between a p-type semiconductor and a metal having a smaller work function: (a) band diagrams before joining; (b) band diagrams for the junction at equilibrium. E_{VAC} is the vacuum energy level, $q\phi_M$ is the metal work function, $E_{F,M}$ is the metal Fermi energy, $E_{F,SC}$ is the semiconductor Fermi energy, $q\chi$ is the semiconductor electron affinity, E_C is the semiconductor conduction band edge, E_V is the semiconductor valence band edge, $q\phi_B$ is the Schottky barrier energy, W is the depletion region and V_0 is the contact potential.

1.3 Shottky and ohmic contacts

In this thesis, a diode-like structure of polymeric materials sandwiched between two metal electrodes is fabricated. It is important to understand the fundamental physics at the semiconductor/metal interface since most electrical properties are related to the contacts, or so called junctions, between semiconductors and metals. When a metal and a semiconductor joined, two possible types of contact can result depending on the types of the metal and semiconductor. The contact may be either rectifying, which only allows current to pass in one direction, or ohmic, in which current can pass in either direction. This section deals with both the rectifying and ohmic contacts, and the discussion is totally around the p-type semiconductor since PFO and PVK are p-type.

Rectifying contact Before discussing the behaviour of a metal- semiconductor contact, it is necessary to introduce the concept of the work function. The work function ($q\Phi$) of a material in the vacuum is the energy required to remove an electron at the Fermi level (E_F), the level of the electrochemical potential for the electrons, to the vacuum outside the material. The values of work functions are very sensitive to surface contamination. Typical values for very clean surfaces are 4.3 V for Al and 4.8 V for Au [26]. When a metal with work function $q\Phi_M$ is brought in contact with a p-type semiconductor having a work function $q\Phi_S$, the transfer of positive charge from the semiconductor to the metal occurs until the alignment of the Fermi levels at equilibrium happens (Figure 1.3). For $\Phi_M < \Phi_S$, the semiconductor Fermi level is initially lower than that of the metal before contact is made. To align the two Fermi levels, the electron energies of the semiconductor must be raised relative to that of the metal. It results in the form of a constant equilibrium potential difference V_0 between the semiconductor and the metal across some region W about the junction. The region W is called the depletion region, and the potential difference V_0 is called the contact potential. Indeed, the transfer of positive charge from the p-type semiconductor to the metal results in a depleted region W at the semiconductor near the junction. W is called depletion region since it is almost depleted of carriers compared with the rest of the semiconductor, and almost only space charge exists within W because of uncompensated acceptor ions. The negative charge due to the uncompensated acceptor ions within W matches the positive charge on the metal. By assuming the negative charge in the metal is a thin sheet of charge to the left of the junction, the depletion width W in the semiconductor is given by:

$$W = \sqrt{\frac{2\epsilon_0\epsilon_r(V_0 - V)}{qN_A}} \quad (1.9)$$

where ϵ_0 is the permittivity of vacuum, ϵ_r is the relative permittivity of the semiconductor, V_0 is the contact potential, V is the external applied voltage, q is the elementary charge and N_A is the density of dopants. Within the depletion region, holes are in transit from one side of the junction to the other. Some holes diffuse from the semiconductor to the metal, and some

are swept by the electric field from the metal to the semiconductor. The equilibrium contact potential V_0 prevents further net hole diffusion from the semiconductor conduction band into the metal and is equal to the difference of work function potentials $\Phi_M - \Phi_S$. By definition, the potential difference V_0 is an equilibrium quantity, and no net current can result from it. It is a built-in potential barrier, which is necessary to the maintenance of equilibrium at the junction; it does not imply any external potential. However, the V_0 can be decreased or increased by the application of either forward- or reverse-bias voltage V across the junction. The Schottky barrier height Φ_B for electron injection from the metal into the semiconductor conduction band is predicted by Schottky-Mott model and is equal to $\frac{E_g}{q} - (\Phi_M - \chi)$, where $q\chi$ is called the electron affinity and is measured from the vacuum level to the semiconductor conduction edge. The Schottky-Mott model predicts the existence of the band bending and the formation of the Schottky barrier in metal-semiconductor junctions. That is why the rectifying contact is also called the Schottky barrier contact. when a forward-bias voltage V is applied to the Schottky barrier of Figure 1.3, the contact potential is reduced from V_0 to $V_0 - V$ Figure 1.4(a). As a result, holes in the semiconductor valence band can diffuse across the depletion region to the metal. This gives rise to a forward current (semiconductor to metal) through the junction. Conversely, a reverse bias increases the barrier to $V_0 + V_r$, and hole flow from semiconductor to metal becomes negligible Figure 1.4(b). In either case flow of holes from the metal to the semiconductor is retarded by the barrier ϕ_B , which is not affected by the bias voltage. The resulting diode current is suggested in Figure 1.4(c). The reverse saturation current (I_0) depends on the size of barrier ϕ_B for hole injection from the metal into the semiconductor. Then, the Schottky barrier diode can rectify, with easy current flow in the forward direction and little current in the reverse direction.

The forward current is due to the injection of the majority carriers from the semiconductor into the metal with no minority carrier injection, and the storage delay time associated with the minority carrier injection is absent in Schottky barrier diodes. Thus, this type of diode is essentially a majority carrier device, and their high-frequency properties and switching speed are generally better than typical p-n junctions.

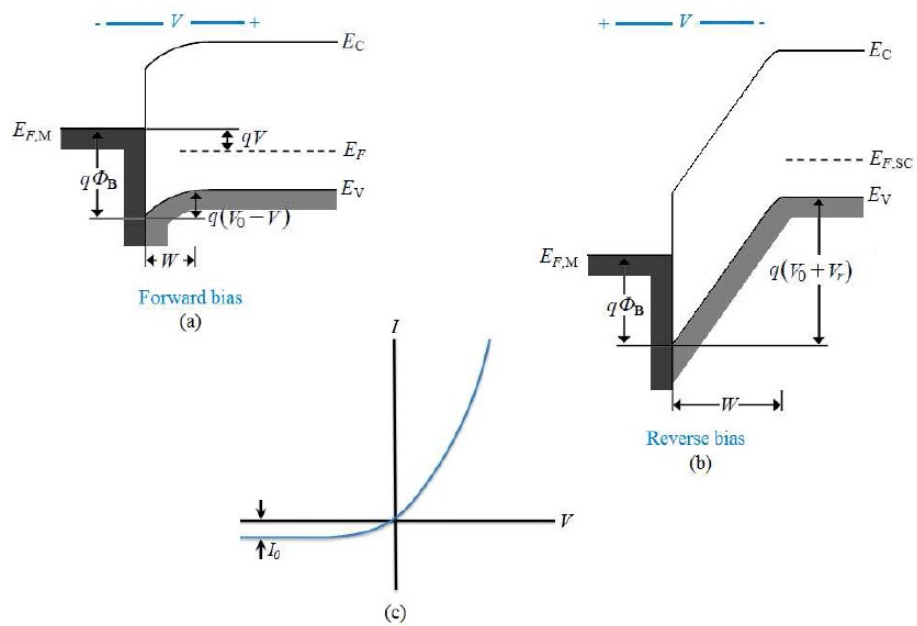


Figure 1.4: Effects of forward and reverse bias on the junction of Figure 1.3: (a) forward bias; (b) reverse bias ($V = -V_r$); (c) typical current-voltage characteristic.

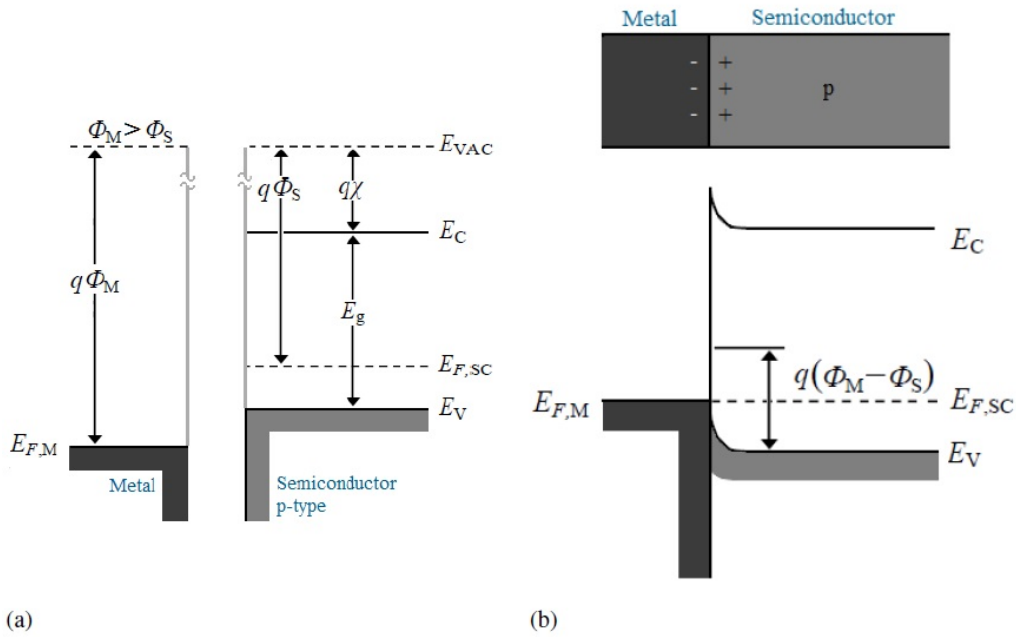


Figure 1.5: Ohmic contact between a p-type semiconductor and a metal having a greater work function: (a) band diagrams before joining; (b) the equilibrium band diagram for the junction.

Ohmic contact It is important that the metal-semiconductor contact which connect the diode to the electronic circuit to be an ohmic contact. This is due to the fact that the ohmic metalsemiconductor contact, which has a linear IV characteristic in both biasing directions, possess minimal resistance and no tendency to rectify signals. For an ohmic metal-semiconductor contact, the charge transfer in aligning the Fermi levels occurs from the metal to the semiconductor. For a p-type semiconductor, this happens when $\phi_M < \phi_S$, where the Fermi levels are aligned at equilibrium by transferring holes from the metal to the semiconductor. This lowers the semiconductor energy levels relative to the metal at equilibrium Figure 1.5. In this case the barrier to hole flow between the metal and the semiconductor is small and easily overcome by a small voltage. Unlike the rectifying contacts, no depletion region occurs in the semiconductor since the electrostatic potential difference, required in Fermi levels alignment at equilibrium, needs that the hole accumulates in the semiconductor.

The Schottky-Mott model correctly predicts the existence of band bending for different semiconductors; however, its prediction of the Schottky barrier height is not compatible with the experimental measurements. In fact, the center of the semiconductor is locked or pinned to the Fermi energy level of the metal due to a phenomenon called Fermi level pinning. Thus, the Schottky barrier height is almost equal to $\frac{E_g}{2}$ and insensitive to the metal and semiconductor work functions. The Fermi level pinning occurs due to chargeable energy states inside the band gap of the semiconductor right at the interface. These energy states either are induced during the direct chemical bonding of the metal and the semiconductor (metal-induced gap states) or are already present on the surface of the semiconductor (surface states).

For organic semiconductors, the Schottky model can be modified by considering the HOMO and LUMO levels instead of the valence and conduction bands, respectively. In addition, the conjugated polymers, as typically used in organic light-emitting diodes or solar cells are undoped semiconductors with trap states. Then, the Fermi level pinning due to interface trap states results in a constant Schottky barrier potential in organic semiconductor-metal interfaces. These properties of the organic semiconductors change the alignment of the energy levels throughout the device. Applying the equation 1.9 for an organic semiconductor, N_A can be equated to the density of free charge n [27]. The undoped polymeric organic semiconductors usually exhibit low density of charge carrier concentrations. Thus, the depletion region can expand throughout the thickness of the semiconductor, according to the equation 1.9. It means that the semiconductor is fully depleted, and the depletion width do not change significantly by biasing voltage. In fact, the organic Schottky diodes should be considered as metal-insulator-metal (MIM) diodes instead of voltage controlled metal-semiconductor diodes. Therefore, when electrodes with different work functions are utilized, a diffusion potential V_d (the counterpart of the contact potential V_0), which corresponds to the work function difference between the anode and the cathode, forms across the undoped semiconductor. Accordingly, the diffusion potential only depends on the nature of the electrodes and not on that of the semiconductor layer. The diffusion potential equals to the barrier height ϕ_B . The anode acts as the ohmic injecting contact, and the cathode acts as the non-ohmic

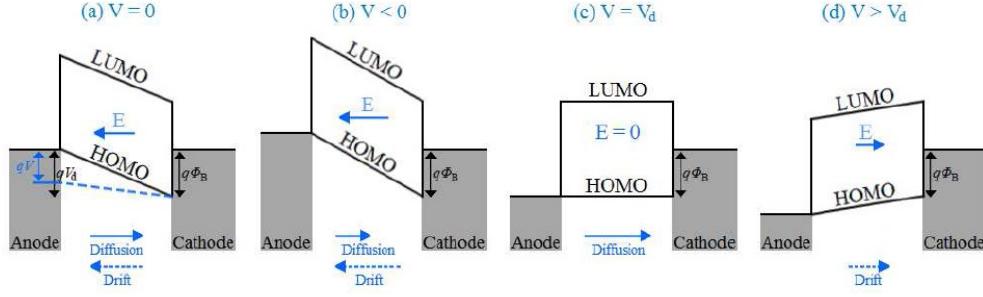


Figure 1.6: Energy diagram of an organic diode with a fully depleted undoped p-type semiconductor for (a) thermal equilibrium and upon applying a small positive bias smaller than the built-in voltage (dashed line), (b) reverse biasing, (c) forward biasing voltage equals to contact potential, and (d) forward biasing voltage greater than contact potential. E is the electric field.

(rectifying) collection contact. In MIM structures, band bending due to the uncompensated dopants is absent. Also, the injected holes at the ohmic contact do not result in band bending at the semiconductor near the interface. In fact, once the organic semiconductor and the metal are brought into contact, the Fermi levels align by transfer of charge from the electrode with higher work function (injecting contact) to the electrode with the lower work function (collection contact). Thus, the energy levels can be illustrated with tilted, rigid energy bands, as depicted in Figure 1.6.

Applying an external biasing voltage can either increase (reverse biasing, Figure 1.6(b)), or decrease (forward biasing, Figure 1.6(c) and 1.6(d)) the injection barrier. When no voltage is applied, the work function difference induces an electric field that inhibits any hole injection at the anode, and the Fermi energy levels of the anode and the cathode align (Figure 1.6(a)). For reverse biasing, this backward electric field increases, so that no current is expected to flow through the diode. The electric field is cancelled by the application of a voltage that exactly compensates the diffusion potential; this corresponds to the situation of flat bands (Figure 1.6(c)). When $V > V_d$, the electric field is reversed and current starts to flow through the diode (Figure 1.6(d)). In fact, the positive charge carriers are transferring from the injecting anode contact to the HOMO of the semiconductor, from where they

move to the rectifying cathode contact. As long as the semiconductor is fully depleted, the electric field is constant across the whole semiconductor. The direction of the electric field determines the slope of the tilted energy levels, and also shows the direction of the drifted charge carriers. However, the diffusion current might occur due to the different concentrations of the charge carriers. Thus, the total current is the sum of the drift and the diffusion of the charge carriers. The performance of the injecting anode contact and the rectifying cathode contact can be improved by manipulating the interfacial layers at the metal-semiconductor interfaces. The manipulation of the interfacial layers modify the relative energy levels of the materials, which in turn either change the Schottky barrier height for cathode interface or enhance the ohmic contact for the anode interface. The practical method for p-type organic semiconductors is the use of a metal contact with higher work function compared with the HOMO level of the semiconductor. The HOMO levels of the organic semiconductors are approximately 5_eV , but the available metals with work functions greater than $5eV$ are limited. Therefore, the utilization of different interfacial layers such as PEDOT:PSS [28], molybdenum oxide [29], and vanadium pentoxide [30] has been studied as a method to increase the effective electrode work functions.

1.4 Current-voltage characteristics

The analysis of the diode current density-voltage (JV) curves is the main method to characterize the rectification property of the diode. In fact, the quality of the diode contacts, rectification ratio, forward current characteristics and charge transport properties can be understood from the JV curves. As shown in Figure 1.6, the conduction of the MIM diode can be divided into three different regimes: reverse current region ($V < 0$), diffusion limited current region ($0 < V < V_d$) and space charge limited current (SCLC) region ($V > V_d$). In reverse biasing, the injection barrier for holes from the cathode to the HOMO of p-type semiconductors is high (Figure 1.6(b)). Therefore, the level of the resulting reverse leakage current is typically low. The latter two current regions are discussed as follows.

Injection and Diffusion limited current As mentioned before, the ohmic contact between a metal and a fully depleted semiconductor can be described as an injecting contact, where the metal injects charges into the insulating material. When the voltage is below (V_d), the gradient of the hole density arises the diffusion of the holes towards the cathode (Figure 1.6(c)), resulting in the injection and diffusion limited current. On the other hand, the hole drift current due to the electric field is negative pointing toward the anode. However, the net current is dominated by the diffusion current, leading to a positive current from the anode to the cathode. The diffusion limited current can be calculated by utilizing the familiar Shockley diode equation; however, this equation is derived to describe a bipolar current through a p-n junction. Thus, Applying this equation to unipolar devices with undoped semiconductors such as organic MIM diodes is questionable. In 2013, Bruynt et al. expressed the below equation for the hole-only diffusion in the MIM type devices:

$$J_{diff} = \frac{q\mu N_v(\phi_B - b - V)(e^{\frac{qV}{kT}} - 1)}{Le^{\frac{qb}{kT}}[e^{\frac{q(\phi_B - b)}{kT}} - e^{\frac{qV}{kT}}]} \quad (1.10)$$

where N_v is the charge-carrier density at the ohmic contact interface, ϕ_B is the barrier height at the rectifying contact, b is the band bending parameter, and L is the thickness of the semiconductor [31]. The derivation was based on the modification of the classical diffusion theory of Schottky to consider an ideal ohmic contact, an undoped semiconductor and the absence of the band bending at the interfaces. The equation 1.10 is almost proportional to V , that is $J_{diff} \propto V$ as Figure 1.7 shows.

Space-charge-limited-current region The concept of the space-charge-limited current (SCLC) model was initially introduced by Mott and Gurney [32]. The main idea for this model is to describe the electronic charge in a material as a uniformly distributed charge system over a region instead of a point charge system. The model applies when one charge carrier dominates the conduction of current in the material, or one carrier is comparatively more mobile than the other, for instance the conduction of holes in forward bias in a p-type semiconductor device [33]. In this case, the number of holes

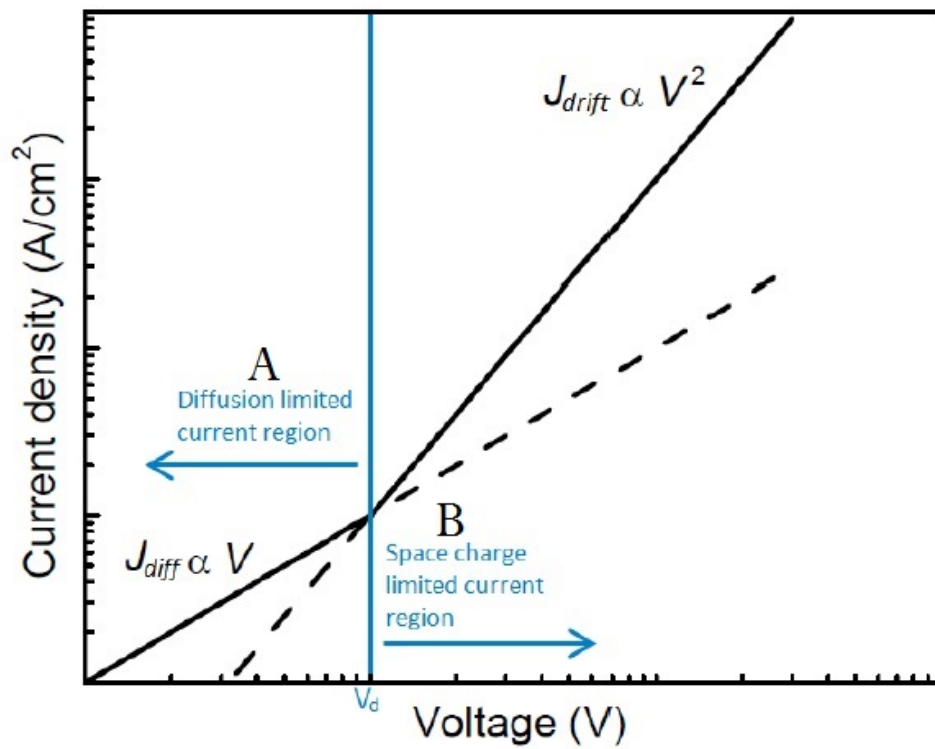


Figure 1.7: Log-log plot of an ideal JV characteristic at forward biasing for an organic diode.

is higher than the number of electrons. Therefore, a space charge region is formed in the material, resulting in the modification of the current [34]. If the concentration of injected carriers is higher than the background carriers, the current-voltage plot will deviate from Ohm's law (region B). Here, the injected carriers start to fill the traps inside the material. The nature of the traps can be divided into two configurations, a single set of traps (shallow or deep traps) and traps distributed in energy space. The presence of traps is found to have an effect on the current [35]. If the material consists of a single set of traps, the current-voltage relationship in region B can be expressed as follows [36]

$$J = \frac{9}{8} \left(\frac{\Theta}{1 + \Theta} \right) \mu \epsilon \frac{V^2}{d^3} \quad (1.11)$$

Where Θ is the ratio between free and trapped carriers and ϵ is the permittivity of the material. The gradient of the $\log(I)$ - $\log(V)$ plot is then equal to two. The situation becomes more complicated when traps are distributed in energy, where equation 2.5 fails to explain the effect of the traps. Mark and Helfrich [37] have proposed a current-voltage relationship based on the idea that the traps are distributed in energy space so that

$$J = N_v \mu e^{1-n} \left(\frac{\epsilon \epsilon_0 n}{N(n+1)} \right)^n \left(\frac{2n+1}{n+1} \right)^{n+1} \frac{V^{n+1}}{d^{2n+1}} \quad (1.12)$$

Where N_v is the effective density of states in the valence band, $n = \frac{T_c}{T}$, where T_c is a characteristic temperature of the distribution of the traps and T is the sample temperature ($T_c > T$). The slope of $\log(I) - \log(V)$ plot, in this case, is greater than two. As the voltage increases, traps are filled by the injected carriers until at a specific voltage where all traps are filled. This voltage is called the trap-filled limit (TFL) voltage, designated as V_{TFL} . After this point, the amount of injected carriers greatly exceeds trapped carriers ($\theta > 1$). Equation 1.11 reduces to the so-called trap-free SCLC relationship [38] and therefore

$$J = \frac{9}{8} \mu \epsilon \epsilon_0 \frac{V^2}{d^3} \quad (1.13)$$

In this case, the gradient of the $\log(I) - \log(V)$ plot is equal to two. The current from equation 1.13 is higher than that from equation 1.11, which means the SCLC diminishes upon the presence of traps in semiconductor.

Chapter 2

Semiconducting polymers

2.1 Introduction

In the last 20 years, under the thrust of the Nobel Prize in Chemistry in the 2000, a growing interest in this research field arose allowing the technological development of organic electronics. Polymers are widely used for inexpensive, disposable products, due to their ease of manufacture, versatility and low cost. Their resistance to electrical conductance makes them excellent materials for the insulation of electrical components. The fundamentals of the molecular interactions in conjugated polymers are different from those occurring in the crystalline inorganic semiconductor system. Polymeric semiconductors can form films with complex morphologies and varying degrees of order and packing modes through the interplay of a variety of non-covalent interactions. The common feature that hands these materials their unique property is that of conjugation: the alternation of single and double bonds between carbon atoms. Their molecular structure consistently presents a backbone along which the carbon (or nitrogen, oxygen, sulfur) atoms are sp^2 -hybridized and thus possess a π -atomic orbital. The conjugation (overlap) of these π orbitals along the backbone results in the formation of delocalized π molecular orbitals, which define the frontier (HOMO and LUMO) electronic levels and determine the optical and electrical properties of the (macro)molecules. The overlap of the frontier π molecular orbitals between adjacent molecules or polymer chains characterizes the strength of the inter-

molecular electronic couplings, which represent the key parameter governing charge carrier mobilities. In crystalline inorganic semiconductors, the three-dimensional character and rigidity of the lattice ensure wide valence and conduction bands and large charge carrier mobilities (typically on the order of several 10^{-2} to 10^{-3} $\text{cm}^2 \text{V}^{-1} \text{s}^{-1}$). In contrast, in organic semiconductors, the weakness of the electronic couplings (due to their intermolecular character), the large electron–vibration couplings (leading to pronounced geometry relaxations), and the disorder effects all conspire to produce more modest carrier mobilities due to charge-carrier localization and formation of polarons; transport then relies on polarons hopping from molecule to molecule (here and in the remainder of the text, “molecule” should also be taken as meaning “polymer chain segment” where appropriate). As a result, the charge carrier mobilities strongly depend on the morphology and can vary over several orders of magnitude when going from highly disordered amorphous films (typically, 10^{-6} to 10^{-3} $\text{cm}^2 \text{V}^{-1} \text{s}^{-1}$) to highly ordered crystalline materials (> 1 $\text{cm}^2 \text{V}^{-1} \text{s}^{-1}$). The nature of charge transport in conjugated polymers is much more complicated than for inorganic semiconductors. Thus, it is very helpful in the beginning to address some of the basic principles of organic semiconductors in order to fully understand the nature of charge transport. However, some well-established concepts from the inorganic semiconductor theory, which were previously described in Chapter 1, are still valid in some main areas, such as the band structure, energy level, energy alignment, band bending, Schottky barrier formation, and the current-voltage characteristics. In this chapter, a description of conjugated polymers and their unique properties will be elaborated in more detail.

2.2 Structural Characteristics

Polymers are large system with many identical repeating units of small molecules or chemical groups. A single small molecule, usually called a monomer, is chemically reacted to create a polymer through a polymerization process. If the system consists of more than two repeat units, it is called an oligomer. If the number of repeated units is large, the system is described as a polymer. In practical terms, it is very difficult to have a long chain

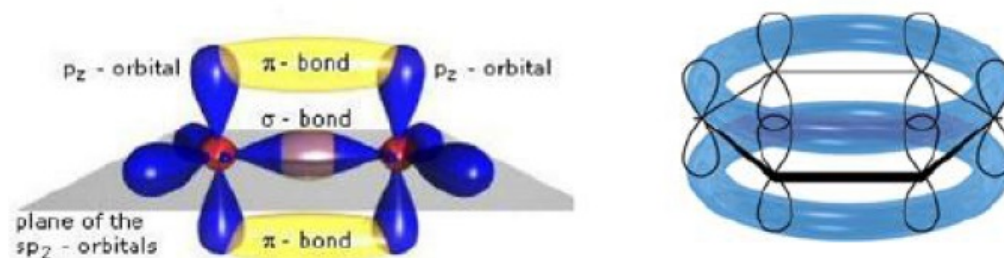


Figure 2.1: Schematic view of σ or π bonds and delocalization of π orbitals in aromatic ring.

with the same number of units. In other words, polydispersity is difficult to control. Conjugated polymers commonly consist of about 104 repeat units in one macromolecular chain. Fundamentally, conjugated polymers comprise only straight chain units or benzene rings with six carbon atoms or a combination of these. In general, the electronic structure of π -conjugated polymers originates from the sp^2, p_z hybridized wavefunctions of the carbon atoms in the repeat unit [?]. Semiconducting polymers are described in terms of the energy bands that originate from the bonding and anti-bonding energy levels associated with the σ -bonds between adjacent carbon atoms (formed from the sp^2 wavefunctions) and the orthogonal π -bonds that originate from the p_z wavefunctions. The σ -bonds hold the structure together, but the π -bonds are the origin of the properties that characterize conjugated polymers as semiconductors. A schematic band diagram for π -conjugated polymers is shown in Figure 2.2. The wavefunctions of the π -bands are linear combinations of the p_z orbitals from the carbon atoms in each repeat unit. In the one-electron approximation (i.e. neglecting the electron–electron Coulomb interaction), the number of sub- π -bands is determined by the number of carbon atoms in the repeat unit of the polymer. The first and classic example of a semiconducting polymer is polyacetylene. The molecular structure and π -electron band structure of trans-polyacetylene are shown in Figure 2.3. The large π -electron bandwidth, $W \simeq 12\text{--}13$ eV, leads to delocalization of the electronic wavefunctions along the conjugated polymer chain. There are two forms of polyacetylene, trans-polyacetylene and cis-polyacetylene. As

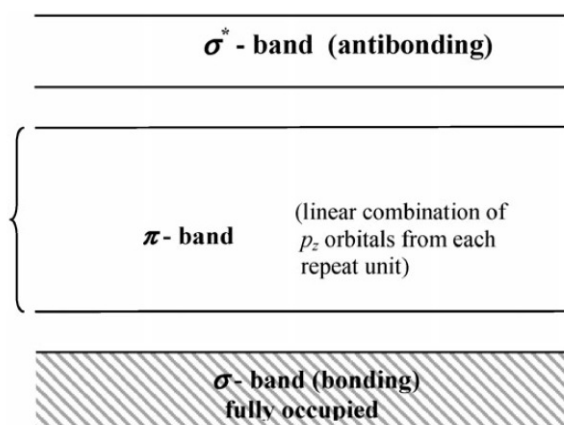
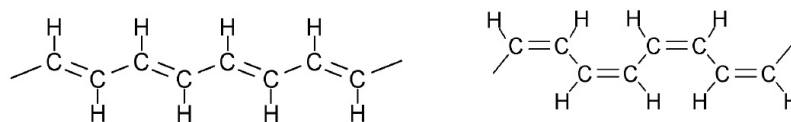
Figure 2.2: Schematic band diagram for π -conjugated polymers.

Figure 2.3: Left: trans-polyacetylene. Right: cis-polyacetylene

shown in Fig. 2.3, for transpolyacetylene, there are two carbon atoms in the repeat unit. As a result, the π -band in trans-polyacetylene is split into two sub-bands (π - and π^* -bands); the π -band is fully occupied and the π^* -band is empty. In cis-polyacetylene, there are four carbon atoms in the repeat unit, and consequently the π -band in cis-polyacetylene is split into four sub-bands with energy gaps in between; the two lower energy π -bands are filled and the two higher energy π^* -bands are empty. The energy of the highest occupied molecular orbital (HOMO) corresponds to the top of the highest energy π -band, and the energy of the lowest unoccupied orbital (LUMO) corresponds to the bottom of the lowest energy π^* -band. The energy gap between the highest occupied energy band and the lowest unoccupied energy band dominates the properties of the semiconductor. In a molecular non-ordered solid the interactions are dominated by weak Van der Waals forces that only slightly perturb the energy levels of isolated molecule; their morphology is usually undetermined or amorphous. Instead, in molecular crystals long range order takes place, therefore a greater energetic shift arises. From the morphological point of view the crystal structure is determined by intramolecular forces and weak interactions, i.e. dipolar, hydrogen bonds or π - π interactions; they are really hard to predict and knowing exactly the structure adopted by a specific compound it's almost impossible.

2.2.1 Conduction mechanisms

The length of the polymer chain, where the alternation between the π and σ bonds is not interrupted, is called the conjugation length [40]. Generally speaking, the conjugation length is the most important structural parameter controlling the charge carrier mobility in a disordered semiconducting polymer system. Charge transport mechanisms in conjugated polymer mainly consist of two processes: intrachain and interchain transport [41]. Intrachain transport (Figure 2.4) is the delocalization of electrons within the polymer backbone and only a small amount of activation energy is required due to a strong interaction between the π -orbitals between neighbouring molecules. In this case, electrons can move freely inside the conjugation length, or in other words electrons can move as long as the conjugation length is not inter-

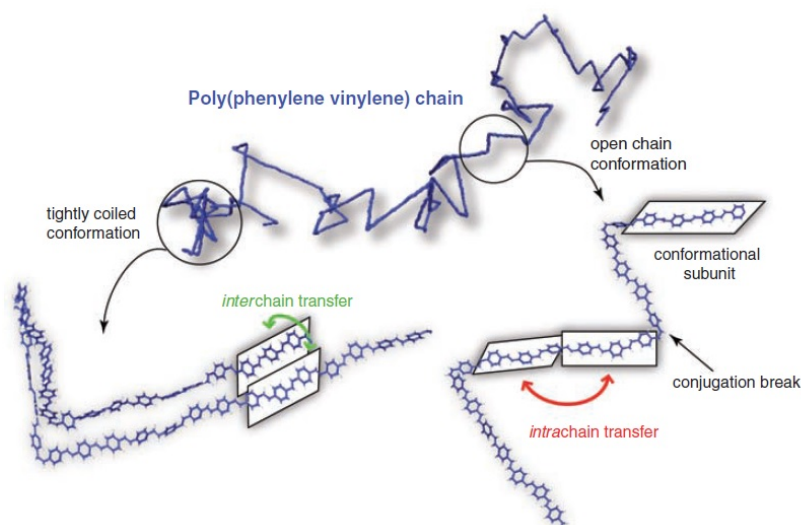


Figure 2.4: Schematic diagram of (right) intra and (left) inter chain transport in conjugated polymers. [39]

rupted. Interchain transport (Figure 2.4(left)), on the other hand, involves the moving of charge carriers between the neighbouring polymer chains and needs more energy to accomplish due to a weak Van der Waals interaction between polymer chains. Interchain transport takes place when the alternation between the σ and π bonds stops. The charge transport mechanism can be explained using a hopping model [42] where electrons or holes "hop" from one chain to another. The efficiency of charge carrier hopping strongly depends on the energy disorder, temperature and the external field. Overall, the inter-molecular transport is the factor that limits the mobility of the whole system.

Polarons The band model is not valid for charge transport in organic semiconductor because it fails to consider a crucial phenomenon in these material which is polarization. In organic solids, the molecular properties dominates that of the crystalline properties due to the weak van der Waals intermolecular interactions. This leads to a tendency of localization of charges on individual molecules. The localized charge, due to a typical residence time, manages to polarize the surrounding electronic and nuclear subsystems. Therefore charge carriers move in the solid not as free particles but they are "dressed"

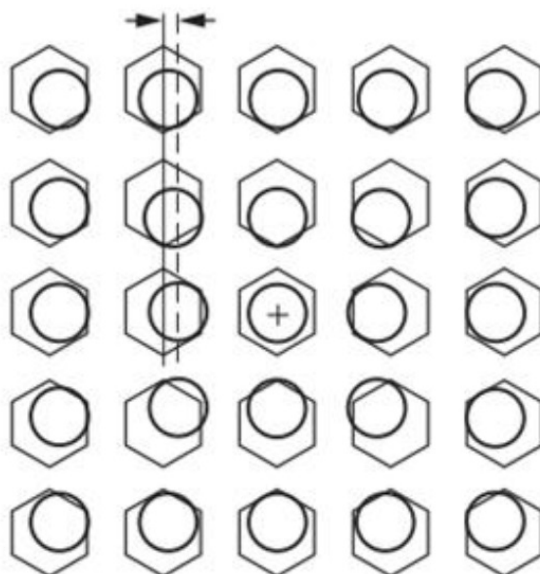


Figure 2.5: The figure is a schematic representation of the formation of a polaron when a positive charge is placed on a molecule in a conjugated organic solid. The hexagons symbolize the core of the nuclei, while the circles represent the delocalized π - electrons.

with a polarization cloud . Such entities are called "polarons". In other words, polarons are quasi-particles deriving from the electron-phonon coupling (or local coupling), i.e. interaction between electrons and quantized modes of vibrational energy arising from atoms' oscillations in the crystal (phonons). The charge carrier mobility of an organic material strongly depends on the electron-phonon coupling, other than on the electronic and phononic bandwidth and phonon energy.

Hopping Transport Charge transport in disordered organic semiconductors such as polymers is dominated by localized states. Charge carriers typically hop between these localized state leading to a diffusive, non-coherent transport with low mobility. Conwell and Mott suggested that in order to overcome the energy between two states the carrier absorbs or emits a phonon. In the case of a constant Density Of State (DOS) at low temperature, hopping over long distances becomes more energetically favorable than hopping to high energies. Hence the conductivity σ varies with temperature

as

$$\sigma \propto \exp \left[- \left(\frac{T_0}{T} \right)^{\frac{1}{4}} \right] \quad (2.1)$$

This is the well-known variable-range hopping model. This model is based on the assumption that charges can hop a short distance with a high activation energy or a long distance with a low activation energy. The temperature dependence of charge transport in such systems is strongly dependent on the density of localized states. Based on this theory Vissenberg and Matters [43] developed a model based on percolation mechanisms. It assumes that transport is governed by the tail states of the Gaussian density of states (DOS) which is approximated by an exponential distribution:

$$N(E) = \frac{N_t}{kT_0} \exp \left(- \frac{E}{kT_0} \right) \quad (2.2)$$

where N_t is the total density of localized states, k the Boltzmann constant and T_0 is the width of the exponential distribution. The resulting mobility gives the following expression

$$\mu = \frac{\sigma_0}{q} \left(\frac{\pi \left(\frac{T_0}{T} \right)^3}{(2\alpha)^3 B_c \Gamma \left(\frac{1-T}{T_0} \right) \Gamma \left(\frac{1+T}{T_0} \right)} \right)^{\frac{T_0}{T}} \left[\frac{C_i^2 (V_G - V_T)^2}{2kT_0 \epsilon_S} \right]^{\frac{T_0}{T-1}} \quad (2.3)$$

Vissenberg and Matters in Ref [43].

Multiple trapping and release The multiple trapping and release (MTR) model is an alternative model which describes transport of charges along the localized levels in the vicinity a delocalized band edge. The basic assumption of this model is that the carriers arrive at a trap with a probability close to one and their release is controlled by thermally activated process. During their transit in the delocalized band, the charge carriers interact with the localized levels through trapping and thermal release 2.6.

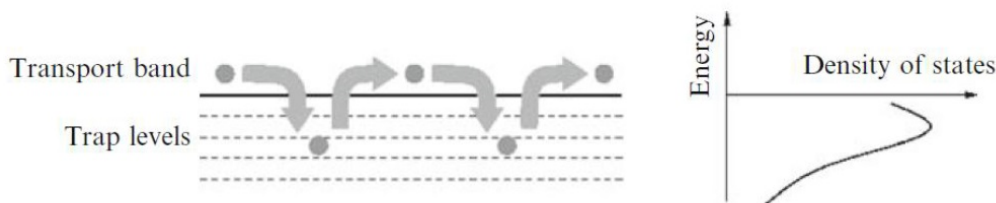


Figure 2.6: Principle of the multiple trapping and release limited charge transport.

2.3 Blend of Nanoparticles in Polymers

Highly ordered polymer nanocomposites are complex materials that display a rich morphological behavior because of variations in composition, structure, and properties on a nanometer length scale. Novel physical properties of soft and bulk polymer nanocomposite materials are also dependent on the supramolecular organization of the nanostructures. The presence of the nanoparticle and the interaction of the polymer with the particle, as well as the particle orientation in a dispersed fluid composition may lead to a variety of ordered composite materials in the bulk or film. Incorporation of metals into polymer matrixes has been shown to produce unique optical, magnetic and dielectric properties at the nano- and macro-scale in nanocomposites, apparently due to the surface and confinement effects of the nanoparticles [44]. The preparation of nanocomposites that comprise polymer shells and magnetic nanoparticles constitutes a very attractive approach since the modular nature of polymeric materials facilitates the design of a wide range of hybrid nanocomposites of various compositions. . On the other hand, among the most frequently utilized techniques to prepare polymer/CNT and/or polymer/clay nanocomposites are approaches like melt mixing, solution casting, electrospinning and solid-state shear pulverization. An important aspect in the synthesis and use of these polymer nanocomposites with nanoparticles is prevention from agglomeration of the NPs.

Spray Pyrolysis method The term “spray pyrolysis” is used in the literature to describe all synthesis processes in which a solution is atomized

and thermolyzed to attain the requisite phase. The spray pyrolysis (SP) method is a very important method for the preparation of metal, metal oxide, non-oxide and composite powders because this method could produce submicron nanoparticles with controlled composition and morphology, good crystallinity, and uniform size distribution, all of which can be readily obtained in only one step. In a typical SP process, a solution is atomized into an aerosol reactor where the droplets undergo solvent evaporation and solute precipitation within the droplet, and then undergo drying, followed by thermolysis of precipitate at a higher temperature, and finally sintering to form final particles. In principle, solution-based aerosol processes, unlike most solution processes, integrate the precipitation, thermolysis (i.e., calcination), and sintering stages of powder synthesis into a single continuous process. In this manner, the advantages of starting with a solution are complemented by providing unique control over the thermolysis and sintering stages of inorganic particle formation. The use of pyrolysis is sometimes too limiting and, in some cases, incorrectly describes the critical thermal process during SP. For example, pyrolysis (i.e., thermal decomposition) does not adequately capture the various oxidation, nitridation, or reduction-based thermal processes that will be increasingly important applications of SP-type processes. Spray Pyrolysis Process Steps are:

1. **PRECURSORS** Aqueous solutions are commonly used due to ease of handling, safety, low cost, and availability of a wide range of water-soluble metal salts. The corrosive nature of the product gases and the adverse effect of residual chlorine on ceramic sintering decreases the general attractiveness of these salts for advanced ceramic powder synthesis, but the technology for handling such systems is available. The physical and chemical characteristics of soluble chemical precursors strongly influence the characteristics of particles formed by SP.
2. **ATOMIZATION** A variety of atomization techniques have been used for solution aerosol formation, including pneumatic (pressure, two-fluid, nebulizers), ultrasonic, and electrostatic. These atomizers differ in droplet size, rate of atomization, and droplet velocity. The velocity of the droplet when it leaves the atomizer is important because it can

determine the heating rate and the residence time of the droplet during SP. The size of the droplets produced with pneumatic or pressure nozzles decreases when the pressure difference across the nozzle is increased. The concept of SP processes is to produce one particle per droplet. Because small particles are required for most advanced ceramic applications, there is a serious need to develop techniques that can atomize large quantities of small droplets at low exit velocities. Indeed, it is for production reasons that companies have used pressure atomizers instead of ultrasonic atomizers. For a specific atomizer, the droplet characteristics depend on the solution density, viscosity, and surface tension. These factors directly affect the droplet size during atomization, and, thus, it is important that the initial droplet size distribution be determined to correlate the particle evolution processes with the initial aerosol.

3. **EVAPORATION PERIOD** During the first stage of SP, the following physical phenomena can occur simultaneously: evaporation of the solvent from the surface of the droplet, diffusion of the solvent vapors away from the droplet in the gas phase, shrinkage of the droplet, change in the droplet temperature, and diffusion of solute toward the center of the droplet. Solute diffusion at high humidities is concluded to be the slowest process, but, at low humidities, the rate of droplet shrinkage may be comparable to the rate of solute diffusion.
4. **DRYING** The drying of droplets containing precipitated salts significantly. When the solute starts to precipitate, the evaporation rate is significantly reduced and the droplet temperature increases steeply until it reaches the ambient temperature.

Chapter 3

Materials and Method

3.1 Introduction

The principles of a variety of experimental techniques employed in the research are thoroughly described in this chapter, ranging from device production to diode characterization. The section begins with a description of the materials used followed by substrate preparation and Schottky diode fabrication. Finally material and device characterisation is then described for the examination of structural, electrical, and radiological properties.

3.2 Materials

PVK is a hole transport material (hole mobility μ_h is much greater than electron mobility μ_{el}) exhibiting an emission spectrum that, owing to the

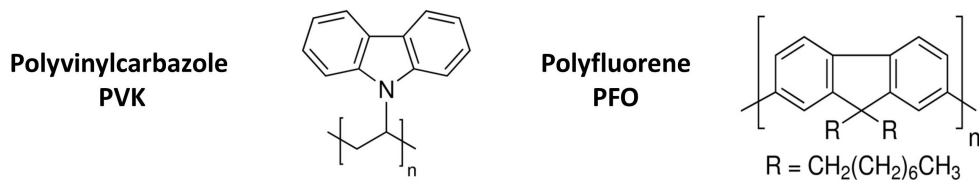


Figure 3.1: Molecular structure of PVK(left) and PFO (right).

properties of carbazole groups, covers the entire blue region [45]. For this reason, recently, PVK is being widely utilized in the fabrication of blue light emitting diodes [46] in the place of conjugated polymers, which present poor emission in blue region, because of their long π -conjugation and relatively low fluorescence quantum yields. Furthermore, more recently, bistable resistance behaviour has been observed in multi-layer structures based on PVK films, renewing the interest on this material also for non volatile organic memory applications [47]. Morphologically, PVK is an amorphous hole conduction polymer, constituted by linear chains of repeated molecular groups $(\text{H}_2\text{C}-\text{HC})_n$, with pendant carbazole side groups $[(\text{C}_6\text{H}_4)_2\text{NH}]$, arranged randomly around the same chain (Fig. 3.1). Such groups act both as chromophores (EL) and hole conducting centres, so that they are mainly responsible for the electrical and electroluminescent properties of PVK. Similarly to what occurs for other polymers, the electrical conduction in PVK is ruled by both field assisted and temperature activated hopping processes, whereas luminescence occurs via radiative decay of a Frenkel exciton. The charge transport in PVK, just as in many other disordered high molecular weight materials, is affected by the presence of impurities that can drastically limit both bulk electrical conduction and charge carrier injection. In particular, the presence of impurities at electrode/ polymer interface strongly affects charge injection mechanisms, inducing localized energy states with charge trapping-detrapping phenomena.

Polyfluorenes are an other promising class of polymers. They are commonly used as blue emissive material in PLEDs or as host component for white emitting copolymers. The wide band gap, however, also complicates the charge injection; it is difficult to achieve efficient injection for both electrons and holes. Especially hole injection can be problematic in polyfluorenes due to the typical deep HOMO level. As an example, poly(9,9-dioctyluorene) (PFO) is an attractive material to function as the blue host material in white light-emitting PLEDs due to its efficient blue emission and high mobility. The HOMO level of PFO, as well as PVK, is located at 5.8 eV below vacuum, leading to a significant hole injection barrier of 0.6 eV when combined with Au which has a work function of approximately 5.2 eV [48].

In this thesis, the charge carrier mobility of PVK and PFO spin coated

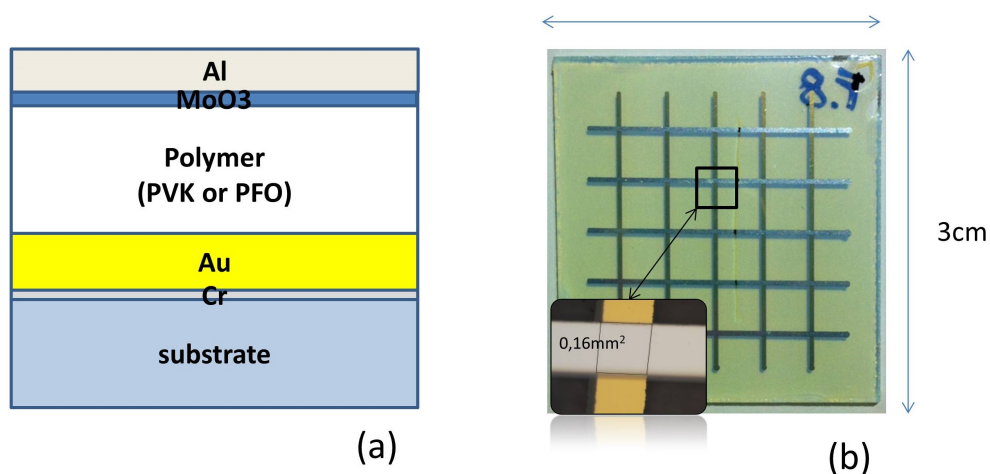


Figure 3.2: Layout of fabricated diodes: (a) schematic cross section showing the different layers; (b) photograph of a cross bar pattern containing an array of 5 x 5 diodes. The inset show a micrograph detailing the area of a single diode.

films have been estimated. By comparing the measured values with the data reported in literature, it has been possible to assess the quality of the obtained films, in order to manufacture prototype X-ray detector and characterize their performances. Such a characterization is necessary in order to optimise device operation, since optimal efficiency and device lifetime can be obtained only by a deep understanding of charge transport and injection restrictions.

3.3 Diode fabrication process

The device fabrication has been performed in the Max Planck Institute for Polymer Research (MPIP) at Mainz. A schematical layout of the fabricated diodes is shown in figure 3.2. Slides of glass were initially cut to a size of 3x3 cm². The substrates were cleaned thoroughly with ultrasonic bath in ultrapure water, acetone and isopropanol to ensure that contaminations was minimized. They were then dried under nitrogen flow. 100 nm of gold on top of 5 nm of chromium were evaporated to create the bottom electrode. The evaporation was performed in a thermal evaporation system COAT 340 *Vactec*(figure 3.3). Depending on the experiments, a different wt% solid con-



Figure 3.3: Thermal evaporator COAT340, Vactec.

tent polymeric solution was prepared by dissolving PVK or PFO in toluene. Both polymers are easy to dissolve in toluene to prepare a solution, and toluene does not react chemically with them. The solution was homogenized by stirring until no solid polymer residue was left. The resulting polymer solution was spin coated with a LabSpin6, SUSS Microtech (figure 3.4) onto the glass substrates at a speed of 1000-4000 rpm for 30 seconds, providing different film thicknesses in relation to the solution concentration and spin speed (rpm) selected. The polymer film was left in vacuum (10^{-3} mbar) at room temperature in a vacuum oven for 12 hours. This process is to ensure that any toluene trapped inside the polymer film is removed. The processing conditions for each PFO thickness are summarized in Table 3.1. Same thicknesses were obtained with higher ratio of PVK in toluene solution. The thickness profile of the active layer was measured using a surface profilometer (Dektak XT, Veeco Instruments) to determine the thickness uniformity of the polymer layer. The surfaces of spin-cast PFO layers were always smooth and uniform, on the contrary the spin-coating of PVK solutions provides wavy surface at concentrations lower than 10wt% with respect to toluene. In that case the measurement uncertainty on the PVK layer thickness is about 10%. In the following chapter the results are calculated taking into account the mean value of the measured thicknesses for the each PVK layer.

Polymer	Solution Concentration wt%	Thickness μm	Spin rpm	Acceleration Speed rpm/s	Spin time sec
PFO	2	0.2	2000	200	30
	3	0.4	2000	200	30
	4.5	0.7	2000	200	30
	5.5	1.1	2000	200	30
	6.5	1.4	2000	200	30
	8.5	2.4	2000	200	30

Table 3.1: Deposition conditions for PFO films

Finally, 10 nm-thick MoO_3 layer and $100\mu\text{m}$ -thick Al layer have been thermal evaporated as hole injection layer HIL (see par. 4.1.1) and top electrode, respectively. Metal contacts were fabricated by mounting the polymer sample in an evaporator (COAT340). A shadow mask comprising of five linear hole with a length of 2 cm and a width of 0.4 mm was employed to make a cross-bar. Therefore, the defined active area of the device is 0.16 mm^2 (figure 3.2b). Either aluminum wire, gold nuggets or MoO_3 powder was placed in a molybdenum boat connected between the electrodes of the evaporator. The system was initially pumped down to 10^{-3} mbar by a rotary pump and 10^{-7} mbar by a turbomolecular pump. A high current was passed through the molybdenum boat in order to thermally activate the evaporation of the metals. When a selected flow rate was reached the evaporator automatically starts the deposition opening the shutter. The metals were thermally-evaporated through the shadow mask until the selected thickness, measured by the thickness monitoring, was reached. Whenever possible automatic process has been used in order to obtain similar electrode thicknesses for each device. Since the MoO_3 could easily react with oxygen, affecting the electronic properties of the device, the entire process has been carried out inside a glove-box. Upon completion of the diode, the samples were stored in vacuum desiccators or oven in the dark and under a dry nitrogen atmosphere to reduce any oxidation effects and to limit dust contamination.

3.4 Diode Fabrication Techniques

3.4.1 Thermal evaporation

Deposition of purified materials is possible with different thermal evaporation techniques in vacuum. The target material is placed into a vacuum chamber and heated utilizing different heating systems. Once the vapor pressure of the heated material exceeds the pressure of the background gases in the vacuum chamber, the material evaporates and condenses on the cooler target surfaces. In this work, thermal evaporation has merely used for coating metal contacts. Thermal evaporation of metals is typically performed under high or ultra high vacuum conditions. This is done for several reasons. First, the evacuation of the chamber reduces the partial pressure of oxygen or other background gases. These gases might contaminate the sample or even react with the heating apparatus. Second, metals usually possess low vapor pressure. Vacuum conditions permits these low vapor pressure materials to evaporate. Finally, the mean free path of the evaporant particles is extended to larger than the source-to-substrate spacing. This allows the source material to travel to the substrate without deflection caused by intermolecular collisions. The mean free path (λ) of a gas (as a collection of particles that collide elastically with each other) is given by:

$$\lambda = \frac{kT}{4\pi\sqrt{2}r^2p} \quad (3.1)$$

where $k[J/K]$ is the Boltzmann constant, $T[K]$ is the temperature, $p[Pa]$ is the pressure, and $r[m]$ is the effective molecular radius of the gas. A typical mean free path for air at room temperature is 65nm . Therefore, the evaporated materials at atmospheric pressure scatter many times with no appreciable traveled distance. This results in the lost of their directionality. Typical pressure for vacuum thermal evaporation falls in the range of $10^{-6} - 10^{-8}[Torr]$. For these pressures, the typical mean free path is on the order of meters or longer. For instance, the mean free path is approximately 5km at $10^{-8}[Torr]$. With this mean free path, the particles of the evaporant material travel in a line-of-sight pattern from the source to the substrate. In addition to the mean free path, the composition of the background gases during the

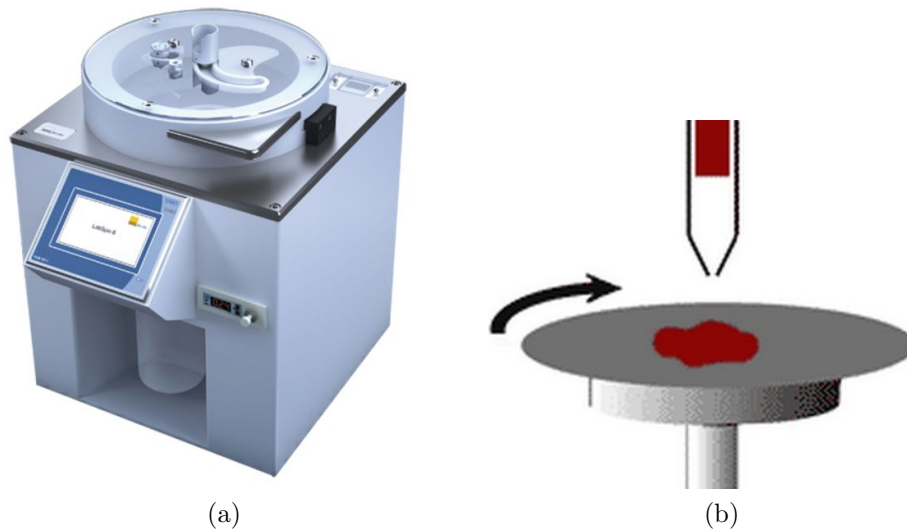


Figure 3.4: (a) LabSpin6, SUSS. (b) Schematic representation of the spin coating process.

deposition exerts a strong influence on the results of the thermal evaporation process. In fact, Some evaporants (especially reactive metals) react with gases which are present in the vacuum chamber. As the evaporant is being heated, its reactions with water, oxygen, hydrogen, and other background gases are accelerated. A clear indication is the reduction in the pressure of the chamber while the material is being evaporated. These reactions could change the properties of the deposited films. For instance, It has been shown that organic semiconductors can be doped by these background gases. It should be noted that additional sources of background gases appear through desorption of gases from the source material, crucible, filaments, and other surfaces in the vacuum chamber, once heating of the source material begins.

3.4.2 Spin-coating

Spin-Coating Overview Spin coating has been used for several decades as a method for applying thin films. A typical process involves depositing a small puddle of a fluid material onto the center of a substrate and then spinning the substrate at high speed (figure 3.4). Centripetal acceleration will cause most of the resin to spread to, and eventually off, the edge of the

substrate, leaving a thin film of material on the surface. Final film thickness and other properties will depend on the nature of the fluid material (viscosity, drying rate, percent solids, surface tension, etc.) and the parameters chosen for the spin process. Factors such as final rotation speed, acceleration, and fume exhaust affect the properties of the coated films. One of the most important factors in spin coating is repeatability, as subtle variations in the parameters that define a spin-coating process can result in drastic variations in the coated film.

Spin-Coating Process Description A typical spin process consists of a dispense step in which the thin films are deposited onto the substrate surface, a high speed spin step to thin the fluid, and a drying step to eliminate excess solvents from the resulting film. Two common methods of dispense are Static dispense, and Dynamic dispense.

Static dispense is simply depositing a small puddle of fluid on or near the center of the substrate. This can range from 1 to 10 cc depending on the viscosity of the fluid and the size of the substrate to be coated. Higher viscosity and or larger substrates typically require a larger puddle to ensure full coverage of the substrate during the high speed spin step. Dynamic dispense is the process of dispensing while the substrate is turning at low speed. A speed of about 500 rpm is commonly used during this step of the process. This serves to spread the fluid over the substrate and can result in less waste of material since it is usually not necessary to deposit as much to wet the entire surface of the substrate. This is a particularly advantageous method when the fluid or substrate itself has poor wetting abilities and can eliminate voids that may otherwise form.

Spin Speed Spin speed is one of the most important factors in spin coating. The speed of the substrate (rpm) affects the degree of radial (centrifugal) force applied to the solution as well as the velocity and characteristic turbulence of the air immediately above it. In particular, the high speed spin step generally defines the final film thickness. Film thickness is largely a balance between the force applied to shear the solution towards the edge of the substrate and the drying rate which affects the viscosity of the solution.

As the solution dries, the viscosity increases until the radial force of the spin process can no longer appreciably move the material over the surface. At this point, the film thickness will not decrease significantly with increased spin time. The SUSS LabSpin6 is specified to be repeatable to within ± 1 rpm at all speeds (max 8000rpm).

Acceleration The acceleration of the substrate towards the final spin speed can also affect the coated film properties. Since the solution begins to dry during the first part of the spin cycle, it is important to accurately control acceleration.

Drying condition The drying rate of the solution fluid during the spin process is defined by the nature of the fluid itself (volatility of the solvent systems used) as well as by the air surrounding the substrate during the spin process. It is well known that such factors as air temperature and humidity play a large role in determining coated film properties. It is also very important that the airflow and associated turbulence above the substrate itself be minimized, or at least held constant, during the spin process. Therefore, the spin-coaters usually employ a cover. There are two distinct advantages to this system: slowed drying of the solution and minimized susceptibility to ambient humidity variations. The slower rate of drying offers the advantage of increased film thickness uniformity across the substrates.

3.5 Electrical Characterization

Electrical characterization has been employed in an attempt to examine the DC electrical characteristics of the diode and identify the conduction mechanism occurred in the device. Electrical characterizations were performed in vacuum ($\sim 3 \cdot 10^{-6}$ mbar) and at room temperature in a customized probe station equipped with micro-probe tips and with a thick metal box to shield the low current (< 1 pA) output signal from environmental electrical noise. Under this condition, the measuring system introduces only a little perturbation on to the diode current. This uncertainty could be neglected with respect to the variability among the device performance. Therefore, it is

not taken into account for the evaluation of the measurement uncertainty. The primary reason of such variability in the measurements is the irregularity of the layer thicknesses. The spin-coating offers the advantage to be a fast and low-cost deposition technique that allows to cover rather large surfaces in air conditions, but at the same time its main drawback is the difficulty to obtain smooth and uniform layers and reduce the bad effects due to the evaporation of the solvent. The I-V measurements were carried out through an HP-4155A, Keysight, by applying a bias voltage from negative to positive connecting the Au contact to the voltage source and the top contacts to the ground. The measurement was completed using a Lab View program. The software allows to control several parameters in order to noise of the IV scan. The aperture time is the period during which the ADC is reading the input signal. In this time a number of current measurements were recorded to give an average value. Resolution, measurement speed, and frequency rejection are functions of the aperture time. The larger the aperture time, the better the resolution. Usually the aperture time is an integral multiple of the period of the mains frequency, in particular the DC sweeps reported in the following chapter (4) have been performed with 20 ms of aperture time. Furthermore, other selectable parameters were the maximum and minimum voltage of the DC sweep. These values have been selected in order to obtain the same electric field for all the devices with different thicknesses. The number of steps per sweep was fixed, in this way also the variation rate of the electric field was kept constant.

3.6 X-ray characterization of fabricated diodes

The diodes were tested under the illumination of X-rays at the Department of Physics and Astronomy of Bologna.

The principle of the technique is based on X-ray induced photoresponse, a phenomenon which is the increase of electrical conductivity when a material is exposed to electromagnetic radiation. (see Chapter 1.) The photoconductivity in organic semiconductors is not so easy as for inorganic materials, owing to the different nature of excitons. An exciton is a bound state of an electron and a hole, which in inorganic semiconductors has a weak binding force (1

meV to 20 meV), and so it can easily dissociate forming an electron-hole pair, while in organic semiconductors the excitonic bond is stronger (between 100 meV and 300 meV). Once generated, the electron-hole pair has an average life time τ , at the end of which the charge carriers are not more available for conduction, due to recombination processes or trapping. Traps states, usually associated with crystal imperfections, dislocations, grain boundaries, and the surface of the material, can hold charge carriers for a certain time, thus possibly causing the enhancement of the recombination probability and a decrease of photocurrent. The conductivity of a semiconductor in darkness condition can be expressed as function of electron and holes concentration, indicated with n and p respectively, as follows:

$$\sigma = e(n\mu_n + p\mu_p) \quad (3.2)$$

where e is the electronic charge and $\mu_{n,p}$ is the electrons/holes mobility. As explained above, when the material is exposed to an electromagnetic radiation with an appropriate energy, the absorption of a photon results in the generation of an electron-hole pair and thus in an increase of the conductivity:

$$\sigma + \Delta\sigma = e[(n + \Delta n)\mu_n + (p + \Delta p)\mu_p] \quad (3.3)$$

Therefore, current density $J = \sigma E$, where E is the electrical field applied, increases to the value:

$$J = (\sigma + \Delta\sigma)E = J_{bulk} + J_{ph} \quad (3.4)$$

Through the measurement of the variation of J in the sample is therefore possible to detect the radiation absorption by the material.

The amount of induced photo current depends on the X-ray dose rate, which is commonly referred to as an energy deposited per unit time, or the applied voltage. The dynamic induced photo current from the diodes was measured at several applied voltages and dose rates. The data for a certain dose rate was corrected with respect to the dark current by subtraction of the dark current to obtain the X-ray induced photocurrent. Dosimetry experiments were completed using 17.5 keV $K\alpha$ X-rays from a commercial

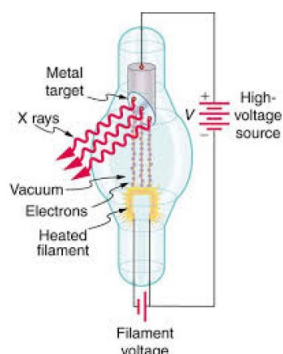


Figure 3.5: Schematic representation of an x-ray tube.

PANalytical PW2285/20 X-ray tube with a Molybdenum target at 35 keV of accelerating voltage and a variable anode current. A shutter is placed in front of the tube to allow an instantaneous (at least for our purpose) opening/closing the beam. The sample was held in a small home build vacuum chamber. The Au contact and metal top contact were connected to a circuit board through a BNC connector for input and output signals by small filament wires. Silver paste (Agar Scientific, UK) was applied to hold the filament wire to the metal contacts. BNC cables connect probes to a Keithley 2600B source-meter. GPIB-USB connection with the computer, and a custom Labview software drives the instruments, composed the acquisition system. Before each measurement, the vacuum chamber was evacuated by means of a rotative pump and filled with nitrogen.

3.7 Fabrication of Nanoparticle Polymer Diodes

The X-ray stopping power of PVK and PFO is relatively low due to their low atomic numbers. In order to improve the X-ray stopping power increasing the performance of the detector, the idea of adding a high atomic number (Z) material in the polymer layer has been pursued. Intaniwet et al. have already reported the enhanced X-ray response of PTAA diode adding Bi_2O_3 NPs. [49]

Tungsten trioxide (WO_3) and Bismuth(III)oxide (Bi_2O_3) nanoparticles were obtained from Nanograde, Switzerland. Briefly the particles were pre-

pared by spray pyrolysis (sec. 2.3) and subsequently dispersed in Toluene using ultrasound and surfactants to create a 20 wt% stock solution. This solution was further diluted and then mixed in several ratio with 7 wt% and 11 wt% polymer contained solution. The solution was homogenized with 30 min of ultrasonic bath and 1-3 min sonic horn treatment. The aim of ultrasonication is to break the aggregation of NPs which can be formed after the mixing. During the sonic horn process the solution was maintained at low temperature thanks to an ice bath. The solution needs the low temperature in order to prevent the polymer from overheating that could damage the polymer properties. The solution was immediately spin coated on the gold bottom electrode after the sonic horn treatment to prevent a new formation of NP agglomerates. It is worth noting that adding NPs changes the solution viscosity, typically resulting in thicker layers and eventually in a reduced homogeneity and uniformity of the surfaces. The layers were dried in a vacuum oven at room temperature for 12 hours. The Al/MoO₃ top electrode was finally thermally evaporated with a COAT340 in a glove-box. The NP-diodes were stored in a nitrogen environment to avoid changing the work function of the MoO₃.

3.8 Structural Characterization

The active layer of the fabricated diodes is composed with two different materials: an organic polymer semiconductor and metal-oxide nanoparticles. The presence of the nanoparticle at the top or bottom surface of the polymer layer, as well as a bad nanoparticle dispersion within the polymer may lead to deteriorate the conduction properties of the diodes and the efficiency of the detector. The nanoparticles added to the polymer tend to create aggregations resulting in a large alteration of the blend viscosity, that could dramatically deteriorate the quality of the spin-casted film. Therefore a detailed structural characterization is required in order to better evaluate the electrical measurements and the X-ray photoresponse.

AFM and SEM images enabled to characterize the surface morphology at different scales and evaluate the phase separation of the solution. In order to clearly observe the NPs within the polymer we also performed TEM, that enables to see the distribution of NPs in the blend. Finally, XRD measurement

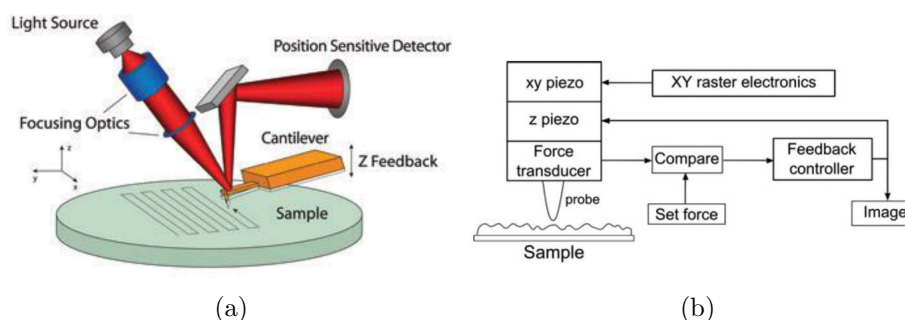


Figure 3.6: (a) General schematics of an AFM. (b) AFM block diagram.[50]

was carried out to evaluate the capability of NP-blend to respond to X-ray radiation and also to evaluate the nanoparticle size distribution.

The sample preparation was changed slightly in relation to the used structural characterization technique. In general, several solutions were prepared varying the NP concentrations with respect to PVK or PFO. After ultrasonication, the solutions were deposited by spin-casting (AFM, SEM, TEM) or drop-casting (XRD). For AFM samples have been employed regular glass substrates, for SEM samples Si die (piece of a Si wafer) in order to increase the image contrast. TEM imaging technique requires thin layer ($\sim 50\text{-}200$ nm) on a copper grid. In this case, the layers of NP blend were spin-cast on top of a PEDOT film in order to easily separate in water the blend layer from the substrate. At the last stage, the obtained film was put on the copper grid. Eventually, XRD films were cast by drop-casting on a Si_xO_y substrate, because of the amorphous structure of this material the XRD measurements does not introduce any characteristic peak due to the substrate.

3.8.1 Atomic Force Microscopy

The Atomic Force Microscopy (AFM) has been used to characterize the morphology and to gain insight on the film surface. This technique allows to measure features in the range from 100nm to 10 μm with high resolution and accuracy. An AFM is quite different from other microscopes, because it does not create an image by focusing light or electrons onto a surface, like an optical or electron microscope. An AFM “feels” the surface atoms with a sharp probe, building up a map of the height of the sample’s surface. A

general picture of an AFM is shown in Fig. 3.6a. AFM has been performed to obtain information on the dimension of the nanoparticles and to evaluate the size of the nanoparticle cluster. To this aim, four devices with several np-concentration were fabricated for both nanoparticle type.

AFM instrumentation The main components of an AFM microscope are shown in Fig. 3.6b: they can be gathered into the AFM stage, the control electronics and a computer to visualize the final surface image.

AFM stage The microscope stage mainly contains the coarse approach mechanism, the x-y-z scanners (or piezos) and the force transducer. An important challenge in AFM design is making a motion control system that allows the probe to approach the surface before scanning. This should happen without crashing the probe on the sample.

Coarse approach mechanism: In the AFM stage there are two separate motion generation mechanism in the z axis: the first is a stepper-motor-drive mechanism with a dynamic range of a centimeter and a resolution of a few microns. The second is the z scanner, which, together with the x and y scanner allows all the three motion of the tip with respect to the surface.

x-y-z scanners: these scanners are piezoelectric materials which convert electrical potentials in mechanical motion. Typically, the expansion coefficient is of the order of 0.1 nm/V. One possible configuration is a disk which gets longer and narrower when a voltage is applied. Another one is a tube, with electrodes inside and outside. Currently, the tube scanner is the most widely used as it is very compact and allows very precise movements.

Force sensor: the force between the AFM tip and the sample is measured by a force sensor. This tool is typically able to detect forces in the range of pN. The optical lever is the most widely used force sensor in AFMs. The principle of it is shown in Fig. 3.7.

This system consists of a laser focused to a spot on the back of a reflective cantilever, the beam is then reflected onto a split photodetector which measures the position of the laser spot. The optical lever magnifies a tiny movement of the cantilever to create a large movement at the photodiode. If a probe, mounted on the front side of the cantilever interacts with the

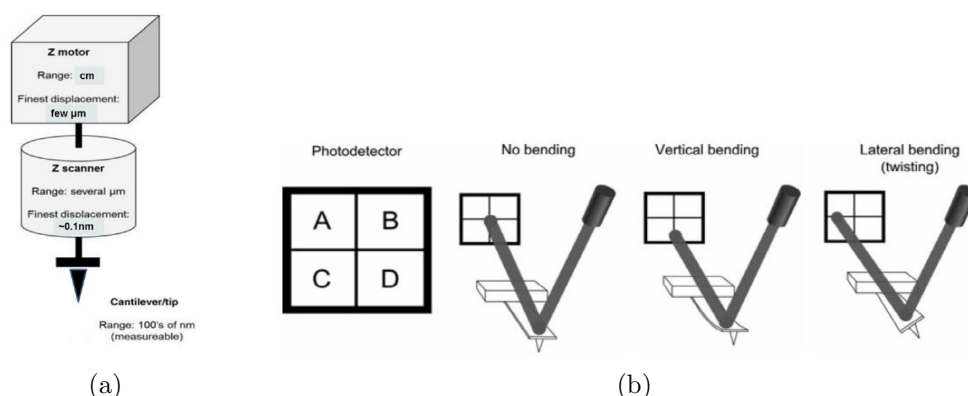


Figure 3.7: (a) Series configuration of the z motor, the z piezo and the probe. (b) The optical lever sensor and an illustration of how the photodetector detects vertical and horizontal bending of the cantilever.[50]

surface, the reflected light path will change. The force is then measured by monitoring the change in light detected by the four quadrants of the photodetector. Specifically, the difference in signal $(A+B)-(C+D)$ gives the vertical deflection of the cantilever, while, $(B+D)-(A+C)$ gives the lateral deflection.

AFM electronics x-y raster pattern: the AFM electronics drive the x-y scanners in a type of raster pattern, as shown in Fig. 3.8a. The x scanner moves across the first line of the scan and back. It then steps in the y direction to the second scan line, moves across it and back, then the third line, and so forth. AFM data are typically collected in only one direction, called the fast scan direction: the x axis in our case. The y direction is called, on the other hand, the slow scan direction. While the x scanner is moving across a scan line, the image data are sampled digitally at equally spaced intervals. The spacing between the data points is called the step size which results in the full scan size divided by the number of pixels. The number of lines in a data set usually equals the number of points per line, thus, the typical data set is made up of a square grid.

Feedback control: the feedback control is used to maintain a set force between the probe and the sample. The control electronics takes the signal from the force sensor and uses it to drive the z piezo so as to maintain the probe-sample distance, and thus the interaction force at a set level.

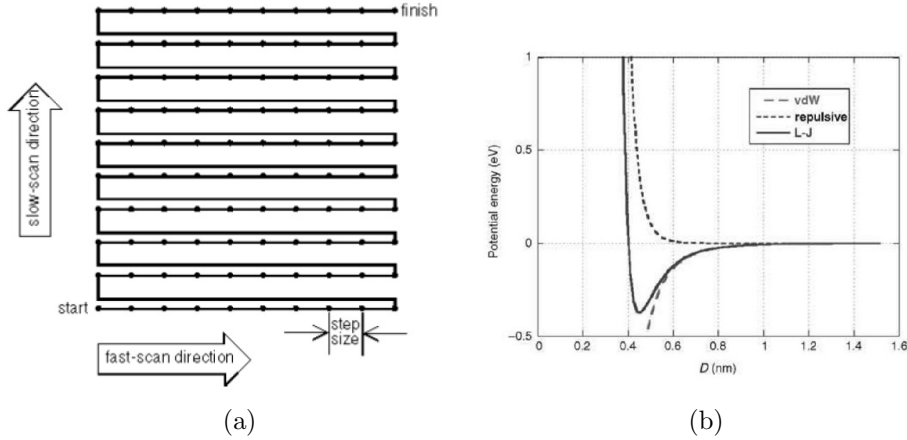


Figure 3.8: (a)x-y scanner motion during data acquisition. (b)Distance dependence of the Lennard-Jones potential.

Interactions in AFM The most common potential used to describe the interaction between the tip and the substrate is the Lennard-Jones potential:

$$V_{LJ}(r) = \epsilon \left[\left(\frac{\sigma}{r} \right)^6 + \left(\frac{\sigma}{r} \right)^{12} \right] \quad (3.5)$$

where ϵ is basically the depth of the potential well and σ is the finite distance at which the potential is zero. This potential is the sum of two physical interactions between the tip and the substrate's atoms. One is an attractive contribution, commonly called van der Waals potential; this contribution is mainly relevant at big distances. The second part, instead, is a repulsive potential directly connected with the Pauli exclusion principle: this contribution has main effects at short distances.

AFM modes A very large number of possible modes of operation are nowadays used in AFM. Among them, contact mode and tapping mode are one of the most relevant.

Contact mode Contact mode was the first mode developed for AFM. It is the simplest mode and the basis for the development of the later modes. To understand this AFM mode, it is necessary to use the so called force-distance curve, like the one in Fig. 3.9.

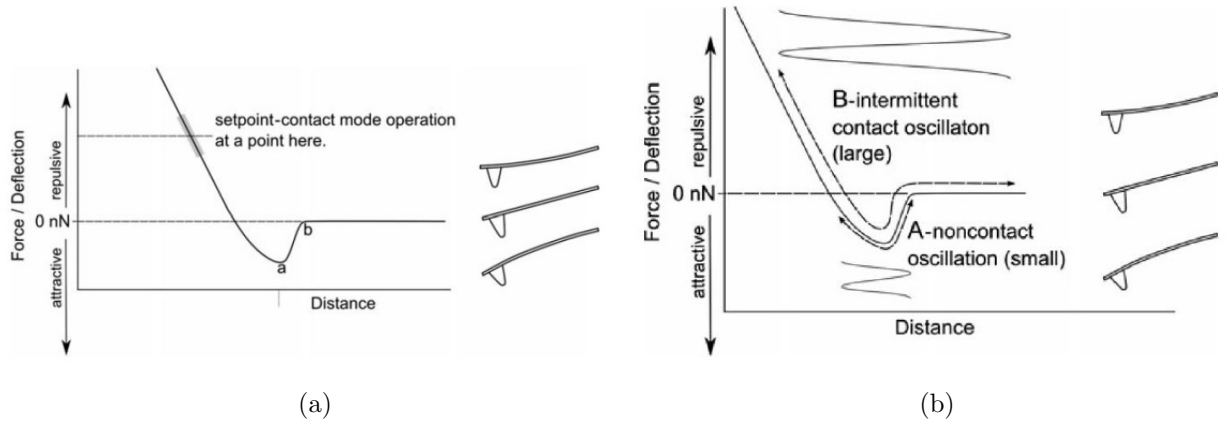


Figure 3.9: (a) Simplified force-distance curve showing contact scanning regime (repulsive region). Right: illustration of probe bending in each regime: repulsive force regime, zero deflection regime and attractive force regime. [50] (b) Different operating regimes for oscillating AFM modes. A: with a small amplitude of oscillation the probe can be kept in the attractive regime. B: with a larger oscillation the probe moves both in attractive and repulsive regime

Considering the approach curve in Fig.3.9, when the tip is far from the sample, the cantilever is considered to have zero deflection. As the tip approaches the sample, it normally feels first an attractive force; as the instrument continues to push the cantilever towards the surface, the interaction moves into the repulsive regime. It is within the repulsive regime that contact mode imaging usually occurs. The basis of contact mode AFM is that the microscope feedback acts to keep the cantilever deflection at a certain value determined by the instrument operator. This point is known as set point and the correspondent imaging mode is called constant force contact mode AFM.

Probably the best reason to use this mode of operation is its high resolution and fast speed.

Tapping mode If in contact mode the tip sample interaction is measured following the cantilever's deflection, in tapping mode, one of the possible dynamic mode of operation, the oscillation amplitude of the cantilever, the

frequency and the phase shift may be recorded. This opens several channels for simultaneous data acquisition, each of them describing a different property of the sample. Moreover, since in tapping mode the cantilever is oscillating, the sample damage is substantially reduced. Basically, in this AFM mode, the cantilever is oscillated, usually with an additional piezoelectric element, and typically at its resonance frequency. When the oscillating probe approaches the sample surface, the oscillation changes due to the interaction between the tip and the surface itself. The effect is a damping of the cantilever oscillation, which leads to a reduction in the frequency and amplitude of oscillation. The oscillation is monitored by the force sensor and the z scanner adjusts the z height via the feedback loop to maintain the probe at a fixed distance from the sample. The only real difference between the various oscillating modes are in the amplitude of oscillation applied to the probe. Using a small oscillation amplitude it is possible to maintain the cantilever only in the attractive regime, dominated by the van der Waals potential. This technique is known as non contact mode. On the other hand, it can be seen that if a large oscillation amplitude is applied, then the probe will move, during an oscillation, both in the attractive and repulsive regime. This technique is known as tapping mode AFM.

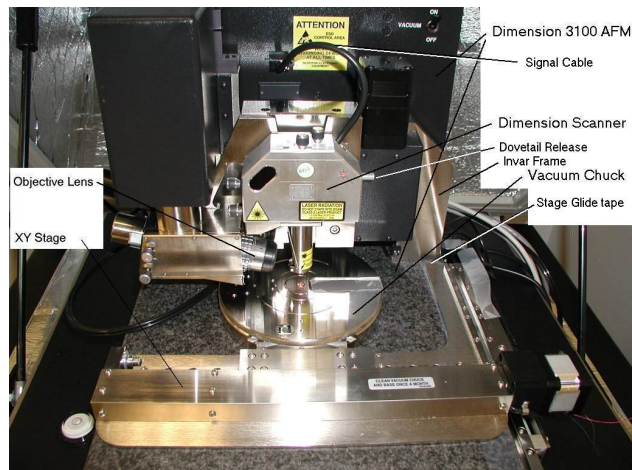


Figure 3.10: AFM Nanoscope 3100

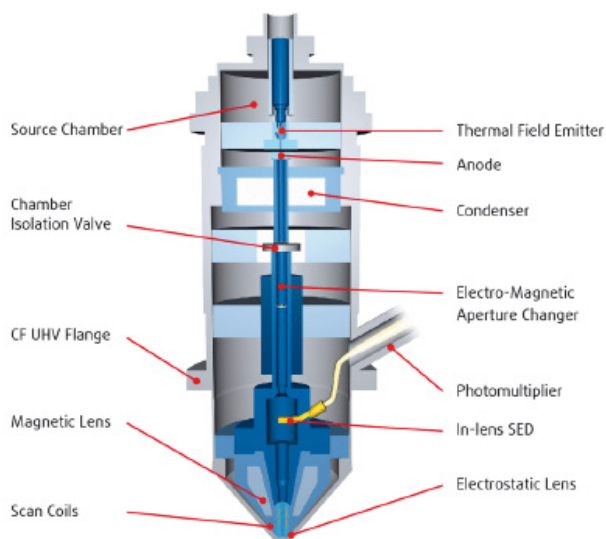


Figure 3.11: Schematic diagram showing the main components of a scanning electron microscope.

AFM Experimental setup Throughout this thesis, the morphological investigations are based on AFM operating in tapping mode. We used a Digital Instruments Nanoscope 3100 AFM (3.10).

3.8.2 SEM

The scanning electron microscope (SEM) uses a focused beam (figure 4.14) of high-energy electrons to generate a variety of signals at the surface of solid specimens. The signals that derive from electron-sample interactions reveal information about the sample including external morphology (texture), chemical composition, and crystalline structure and orientation of materials making up the sample. In most applications, data are collected over a selected area of the surface of the sample, and a 2-dimensional image is generated that displays spatial variations in these properties. Areas ranging from approximately 1 cm to 5 microns in width can be imaged in a scanning mode using conventional SEM techniques (magnification ranging from 20X to approximately 30,000X, spatial resolution of 50 to 100 nm).

Accelerated electrons in an SEM carry significant amounts of kinetic energy, and this energy is dissipated as a variety of signals produced by electron-sample interactions when the incident electrons are decelerated in the solid sample. These signals include secondary electrons (that produce SEM images), backscattered electrons (BSE), diffracted backscattered electrons (EBSD that are used to determine crystal structures and orientations of minerals), photons (characteristic X-rays that are used for elemental analysis and continuum X-rays), visible light (cathodoluminescence–CL), and heat. Secondary electrons and backscattered electrons are commonly used for imaging samples: secondary electrons are most valuable for showing morphology and topography on samples and backscattered electrons are most valuable for illustrating contrasts in composition in multiphase samples (i.e. for rapid phase discrimination). X-ray generation is produced by inelastic collisions of the incident electrons with electrons in discrete orbitals (shells) of atoms in the sample. [51]. As the excited electrons return to lower energy states, they yield X-rays that are of a fixed wavelength (that is related to the difference in energy levels of electrons in different shells for a given element). Thus, characteristic X-rays are produced for each element in a mineral that is "excited" by the electron beam. SEM analysis is considered to be "non-destructive"; that is, x-rays generated by electron interactions do not lead to volume loss of the sample, so it is possible to analyze the same materials repeatedly.

3.8.3 TEM

Transmission Electron Microscope A Transmission Electron Microscope produces a high-resolution, black and white image from the interaction that takes place between prepared samples and energetic electrons in the vacuum chamber. Air needs to be pumped out of the vacuum chamber, creating a space where electrons are able to move. The electrons then pass through multiple electromagnetic lenses. These solenoids are tubes with coil wrapped around them. The beam passes through the solenoids, down the column, makes contact with the screen where the electrons are converted to light and form an image. The image can be manipulated by adjusting the

voltage of the gun to accelerate or decrease the speed of electrons as well as changing the electromagnetic wavelength via the solenoids. The coils focus images onto a screen or photographic plate. During transmission, the speed of electrons directly correlates to electron wavelength; the faster electrons move, the shorter wavelength and the greater the quality and detail of the image. The lighter areas of the image represent the places where a greater number of electrons were able to pass through the sample and the darker areas reflect the dense areas of the object. These differences provide information on the structure, texture, shape and size of the sample. To obtain a TEM analysis, samples need to have certain properties. They need to be sliced thin enough for electrons to pass through, a property known as electron transparency. Samples need to be able to withstand the vacuum chamber and often require special preparation before viewing. Types of preparation include dehydration, sputter coating of non-conductive materials, cryofixation, sectioning and staining.

Differences between SEM over TEM include:

- In terms of magnification and resolution, TEM has an advantage compared to SEM. TEM has up to a 50 million magnification level while SEM only offers 2 million as a maximum level of magnification. The resolution of TEM is 0.5 angstroms while SEM has 0.4 nanometers

However:

- Large specimens (200 mm diameter wafers, or even larger in specially adapted SEMs), compared to just 2.3 mm or 3 mm in diameter for TEM.
- SEM permits non-destructive evaluation of the specimen (TEM is effectively a destructive technique because of the specimen preparation required).
- Very short specimen preparation time (maybe only a few seconds) while the specimen is attached to a “stub” (specimen holder). TEM specimen preparation is more complex and timeconsuming.

Chapter 4

Results

Introduzione This chapter presents the research results of this thesis. The first subchapter describes the findings about diodes containing only semiconducting polymer as active layer. The second chapter then reports about the diodes containing a composite of semiconducting polymer and nanoparticles. Both sub-chapters are similar in structure to facilitate comparison between the two of them. When necessary findings of the first subchapter are used as reference in the second chapter to understand better how nanoparticles alter the diode properties. The second chapter contains a detailed morphological investigation of the NP polymer composite.

4.1 Pristine PVK and PFO diodes

Introduction In this chapter results on the pure polymer diodes are reported. The first sub-chapter describes the electrical characteristics of the devices and develops a model about the rectified charge transport in them. Subsequently we investigate the x-ray detection properties. Diode parameters which have been varied are: (i) semiconducting polymer (PVK and PFO) and (ii) layer thickness. The findings are summarized and discussed in the end of the chapter.

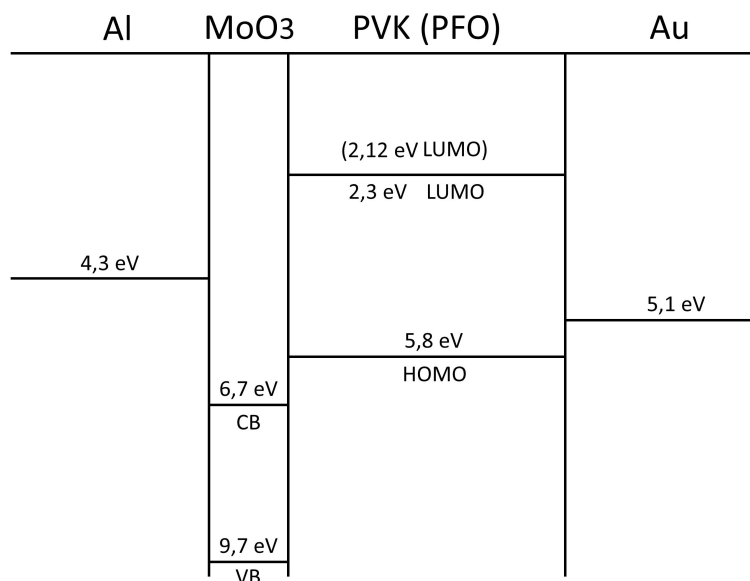


Figure 4.1: Schematic energy band diagram of the fabricated diodes.

4.1.1 Electrical characterization

Current-voltage characteristics of PFO and PVK diodes have been examined to investigate the effect of the differences between the two polymers and to relate the findings to later x-ray detector properties. The I-V characteristics of a polymeric diode are expected to show rectification: low leakage current in reverse bias and a high current in forward bias. For detector applications, a low leakage current at high electric field strength is desirable in order to maximize the current from the drifting charge carriers and to maximize the signal to noise ratio. Therefore it is necessary that our diodes exhibit a relatively good rectifying behaviour for radiation detection applications.

Energy band diagram In order to better understand the highlighted processes of conduction and rectification, we can evaluate the band diagram of the diode. Figure 4.1 depicts energy band diagrams of the Al/MoO₃/PVK(PFO)/Au diodes explaining rectifying behaviour in which the favoured direction involves transport of holes from the Al/MoO₃ electrode to the gold electrode. The HOMO and LUMO values for the polymers are estimated to be situ-

ated at approximately 5.8 eV, 2.3eV for PVK and 5.8 eV, 2.12eV for PFO. Since PVK and PFO behave as a p-type semiconducting polymer, the Fermi level is located close to the HOMO level. In the Al/MoO₃/PVK(PFO)/Au diode, the work function of the Au is lower than the HOMO of the polymer. Therefore it is favourable for a Schottky contact to form at the polymer/Au interface, rendering the injection of holes difficult. Regarding the Al/MoO₃/polymer interface, the role of MoO₃ is to increase the injection of holes (HIL) from the Al contact. Its working mechanism is generally ascribed to the formation of an interfacial dipole and consequently a reduction of the injection barrier. In particular, the Fermi level results pinned against the conduction band minimum, indicating a strongly n-type material. The hole injection of MoO₃ into the semiconductor was described to proceed by electron extraction from the HOMO of the semiconductor through the conduction band of MoO₃. [48]

I-V characteristics The IV curves of the diodes can depict how the quality of the contacts at the anode and the cathode interfaces affect the performance of the diodes. Since the work function of hole injecting electrode is close to the HOMO level of PVK(PFO), it acts as an Ohmic contact. Therefore, the conduction of holes is only limited by the bulk properties of polymers, not by barriers at the metal-polymer interface. In the low voltage regime, the current depends linearly on the applied voltage ($x=1$) and the current-voltage relationship therefore obeys Ohm's law. The current at low voltage is controlled by the Al/MoO₃ polymer interface since this interface forms an Ohmic contact. A transition region arises due to the superposition of the Ohmic current and the space-charge-limited-current. At relatively high forward voltages, when the concentration of the injected charge carriers exceeds the thermally generated free charge carriers, the current becomes proportional to $V^{4.0}$ for PVK and to $V^{2.8}$ for PFO. The values of exponents are calculated from the fitting of the current in forward region at high voltages, the linear fit for different thick devices are shown in figure 4.3. Figures 4.2a, b respectively show the measured Al/MoO₃/PVK(PFO)/Au diode I-V characteristics for diodes with five different thicknesses (from 200nm to 1500nm) of PVK and PFO. The diodes show decreasing current increasing the thickness of polymer layer.

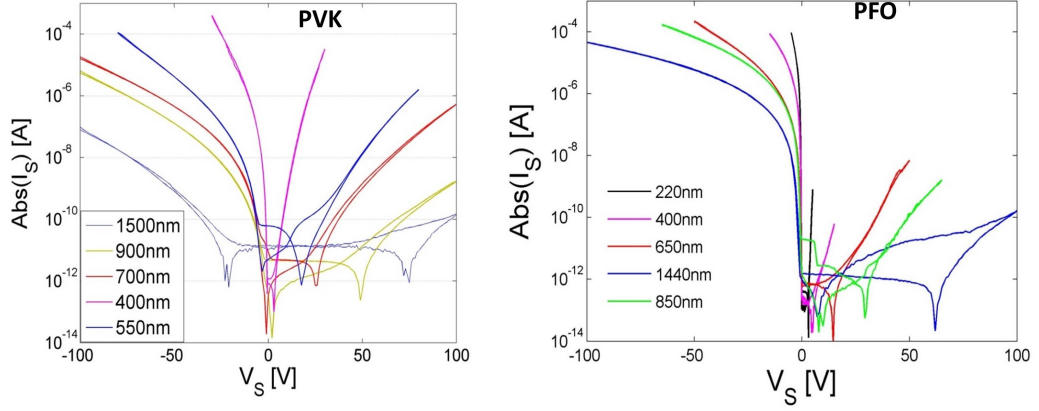


Figure 4.2: Al/MoO₃/PVK(PFO)/Au diode I-V characteristics.

For thick layer, the leakage current in reverse becomes small enough for detection application (increasing SNR). The fabricated diodes with $1.5\mu\text{m}$ -thick polymer layer show for both polymers a low current density of 100.8 nA/cm^2 at $+100\text{ V}$ ($7 \cdot 10^6\text{ V/m}$) in reverse bias. The rectification factor results to be $3 \cdot 10^5$ for Al/MoO₃/PFO/Au, which is significantly higher than that of the Al/MoO₃/PVK/Au diode structure (10^3). The increased rectification in PFO based diodes is associated to the higher mobility increasing the current density in forward direction.

Transport mechanisms Space-Charge Limited Current (SCLC) is a transport regime typical of high resistivity materials, like insulators or organic crystals, which is activated at high electric fields and high charge carriers injection. Thanks to its simplicity it is used to analyse organic semiconducting polymer properties. Several charge-transport parameters like mobility, density of free charge carriers, density of states and energy distribution of traps, can be extracted starting from I-V characteristics.

Figures 4.3 and 4.4 respectively show the plot of $\log(I)$ vs $\log(V)$ and the plot $\log(I)$ vs $\log(L)$, obtained selecting the current of figure 4.2 in the negative bias region (on Au electrode), which means forward operating diodes. In figure 4.3, the linear fits has been calculated fixing a range at high values of electric field, the resulting slopes for each layer thickness are displayed in the legend. The mean value of these slopes is taken into account for further

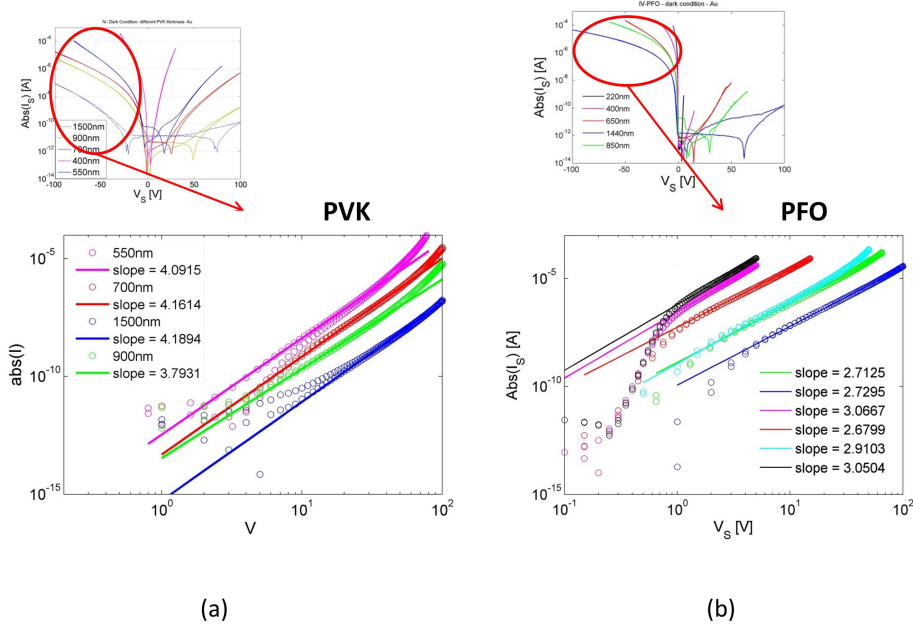


Figure 4.3: Investigation of transport mechanism in polymer diodes: The $\log(I)$ vs $\log(V)$ plot of PVK (left) and PFO (right) allows to extract the exponent of the power-law by performing a linear fit in the forward region at high voltages. .

observations. In figure 4.3, the value of the measured current at a fixed potential is shown in a double logarithmic plot as function of the diode layer thickness. Each point correspond to a different device, it is worth noting the variability of these values at potential and thickness value. This uncertainty is related to the non-uniformity of the film obtained via spin-coating. A linear fit has been calculated taking into account the mean current values of each thickness, the fit curve slope is highlighted in the legend. In figure 4.3(b) are displayed the fitting curves for several voltages, the slope remains approximately constant. Taking into account the equations in paragraph 1.4, the SCLC model can be tested for both device structures. This model can be used to describe the shape of I-V characteristics in forward bias as a power law of $I \sim V^x/L^y$ and to better understand the trap state

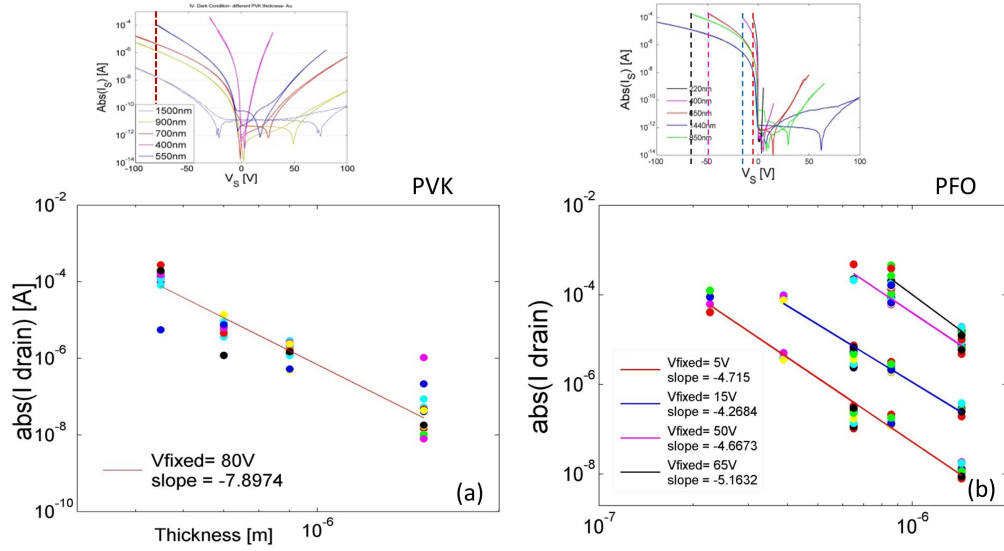


Figure 4.4: Dependence of transport on polymer layer thickness L . The graphs show the $\log(I)$ versus $\log(L)$ plots for PVK (left).

distribution in conjugated polymers. An x exponent of 4.0 ± 0.2 is obtained for PVK and 2.7 ± 0.1 for PFO. From the $\log(I)$ versus $\log(L)$ plots for PVK (left), y results in an y exponent of -7.8 and for PFO (right) which results in an exponent of -4.6 . Both exponents deviate from the SCLC model (eq. ??), which predicts for a trap free material a $\log(J)$ - $\log(V)$ dependence equal to 2 and a $\log(J)$ - $\log(L)$ dependence equal to 3. The trap-filled limit and the trap-free SCLC region cannot be seen in these devices. Instead we suggest to attribute the behaviour to a distribution of traps probably caused by impurities or defects in the chemical structure of PVK (PFO). Another possible explanation for the observation of an exponent > 2 could be offered by a field dependent carrier mobility in the semiconductor.

In order to better explain the extrapolated exponents the model has to be extended as done in the following. First one has to introduce a mobility model that accounts for the most important physical quantities that influence the

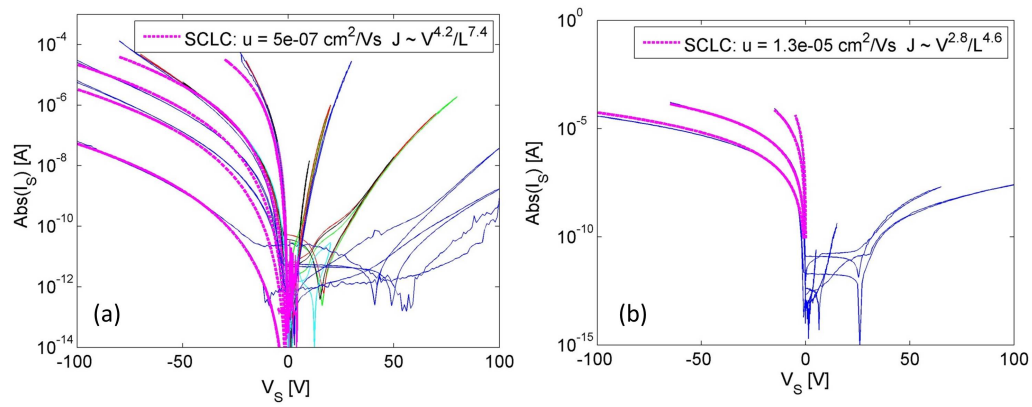


Figure 4.5: Figure 5: Modelling of Diode transport: Measured IV characteristics are compared to modelled data at high forward voltages for both polymers. The transport model [52] takes into account the effects of traps and the dependence of the mobility on the electric field.

$J \sim V^x/L^y$	Extrapolated from log-log plots	Predicted by the model
x	4,0 (PVK) 2,8 (PFO)	4,2 (PVK) 2,8 (PFO)
y	7,8 (PVK) 4,6 (PFO)	7,4 (PVK) 4,6 (PFO)

Figure 4.6: Table of fitting parameters

current transport in organic disordered semiconductors: temperature, carrier concentration, and electric field. The model naturally extends the work of Mark and Helfrich to high electric fields and/or low temperatures regime and leads to a simple analytical expression:[52]

$$J = \sigma_0 \left[\frac{\epsilon_0 \epsilon_r T_0^4 \sin\left(\pi \frac{T}{T_0}\right)}{q(2\alpha)^3 B_c T_F^2 (2T_F - T) T} \right]^{\frac{T_0}{T_F}} \times \left(\frac{2T_0 + T_F}{T_0 + T_F} \right)^{1 + \frac{T_0}{T_F}} \left(\frac{V^{1 + \frac{T_0}{T_F}}}{L^{1 + \frac{2T_0}{T_F}}} \right) \left(\frac{T}{T_0 + T_F} \right)^{\frac{T_0}{T_F}} \quad (4.1)$$

where $T_F = \{T^\beta + [\gamma q F_{eff}/(\alpha k_b)]^\beta\}^{\frac{1}{\beta}}$, β γ are fitting parameters, F_{eff} is an effective electric field, α^{-1} is the effective overlap parameter, T_0 is a parameter that depends on the material disorder and B_C is the critical number for onset of percolation. A good fit is obtained with power-law exponents matching between experimental and modelled data (see figure 4.6). From the model the hole mobilities of the polymers are found to be 1.3e-5 cm²/Vs for the PFO, in excellent agreement with literature value, and 5e-7 cm²/Vs for PVK.

4.1.2 X-ray detector properties

In order to assess the x-ray photoresponse of the fabricated polymer diodes, a constant bias was applied to the gold electrode while the aluminium electrode was grounded. In forward operation a voltage of +100V was used while in reverse operation a voltage of -100 V was applied. The resulting cur-

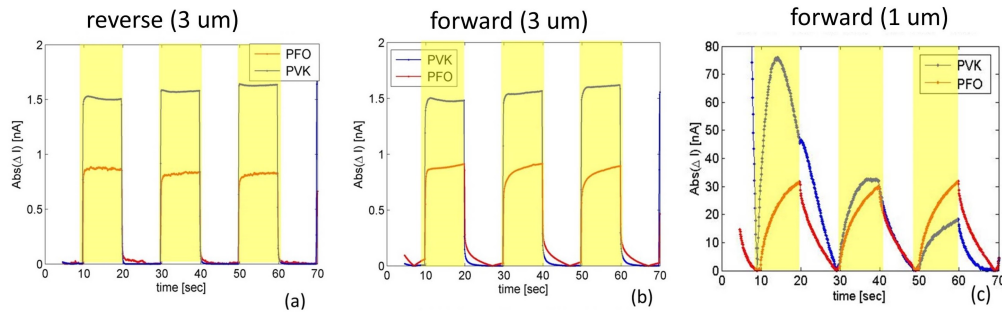


Figure 4.7: Characteristic X-ray photocurrent as a function of time in PVK (blue) and PFO (red) polymer diodes: (a) 3 μm film thickness, reverse bias; (b) 3 μm film thickness, forward bias; (c) 1 μm film thickness, forward bias. Yellow colour marks the time intervals in which the x-ray shutter was open.

rent was continuously monitored. At specific time intervals the shutter of a Mo X-ray tube was opened for 10 sec. The experiment was repeated at least 3 times to probe the stability of the measured response. Characteristic X-ray responses for different devices are depicted in Fig. 4.7. for diodes containing either PVK or PFO. The figures illustrates in particular the impact of diode thickness and mode of operation on the shape of the X-ray response: In Fig. 4.7a a fast, box-shaped response to X-ray exposure is observed for both devices containing thick (3 μm) polymer films when operated in reverse. In this regime the response is larger for the PVK based diode. Fig. 4.7b shows the same devices, but now operated in forward bias. Here the background current has been subtracted for clarity. Again an almost rectangular shape is observed and the magnitude of the signal remains unchanged for both polymers. However for PFO a slow but steady increase of photocurrent is observed during exposure and a slow decrease after exposure. For diodes with thinner polymer films (1 μm), the photocurrent signal changes completely as shown in Fig. 4.7a when operated in forward. Now a “saw-tooth” like shape emerges when the x-ray shutter opens featuring a fast initial increase in photocurrent which slows down and starts to saturate. The magnitude of the photoresponse increases by more than an order of magnitude in comparison to the aforementioned experiment. After shutter closure, the current shows initially a fast decrease, but slows down to return slowly to the background

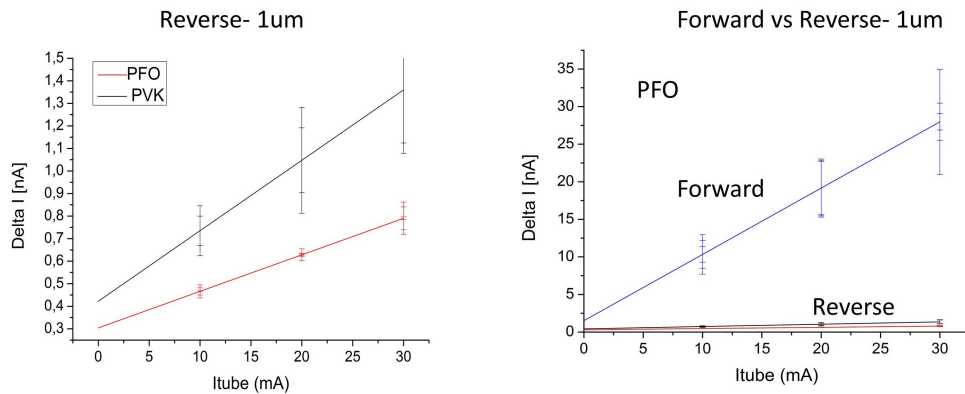


Figure 4.8: Dose-rate dependence x-ray photocurrent response for 1 μm thick diodes: (a) comparison PFO and PVK both operated in reverse; (b) comparison PFO operated in forward and reverse. 4.9.

level. This behaviour is observed in both materials. In PVK it is initially very strong but unstable and finally decreases to a response which is smaller than the very stable PFO response. In conclusion two different regimes of photocurrent and a transition between the two of them is observed. In the first regime the response is fast but photocurrent values are low. In the second the photocurrent is slow and follows a saw tooth shape. In this regime photocurrent values are an order of magnitude larger.

The photoresponse of the diodes was further characterized at different x-ray dose rates (60 mGy/s, 40 mGy/s and 20 mGy/s) which was achieved by adjusting the filament current (30 mA, 20 mA and 10 mA, respectively). The variation in current before closure of the x-ray shutter was taken as the response ΔI . In Figure 4.8 these values are plotted as a function of the filament current for diodes of 1 μm thickness and for operation in forward and reverse regime. All plotted regimes show a linear response and from the slope of the linear fit, the x-ray sensitivity S was extracted. The largest slope is observed for the PFO diode operated in forward regime as shown in Fig 4.8b. The numerical values for the sensitivities of these set of devices are listed in Fig. 4.9. The best sensitivity in reverse operation amounts to 22 ± 5 nC/Gy for the PVK diode of 1 μm thickness. The performance of PFO diodes is slightly lower. No increase in sensitivity is found upon increasing

the thickness of the diodes instead sensitivities even slightly reduce. To compare these values to literature, they have to be scaled by the area of the diode. For the best performing PVK diode in reverse operation one obtains a value of $S = 137.5 \text{ nC/Gy/mm}^2$ (area 0.16 mm^2). This compares to 1.28 nC/Gy/mm^2 as found for PTAA diodes (area 25 mm^2) as reported by Sellin. Importantly for the diodes reported in literature no intermediate layer was applied to facilitate charge extraction at the low work-function electrode. In forward operation the measured sensitivities increase by more than an order of magnitude and for the more stable PFO device we obtain a value of $441 \pm 120 \text{ nC/Gy}$. Scaled to the area this amounts to 2.8 uC/Gy/mm^2 and is unmatched by literature results.

Polymer	bias	Sensitivity
PFO $3\mu\text{m}$	forward	$(12\pm 1)\text{nC/Gy}$
	reverse	$(8\pm 2)\text{nC/Gy}$
PVK $3\mu\text{m}$	forward	$(19\pm 3)\text{nC/Gy}$
	reverse	$(15\pm 4)\text{nC/Gy}$
PFO $1\mu\text{m}$	forward	$(441\pm 120)\text{nC/Gy}$
	reverse	$(13\pm 2)\text{nC/Gy}$
PVK $1\mu\text{m}$	forward	$(500\pm 180)\text{nC/Gy}$
	reverse	$(22\pm 5)\text{nC/Gy}$

Figure 4.9: X-ray sensitivities of Figure 4.8: x-ray sensitivities of polymer diodes at forward and reverse operation for two different thicknesses.

4.1.3 Discussion and conclusion

As detailed in the previous section the electrical characteristics of the fabricated diodes are in qualitative agreement with earlier reported findings on rectifying polymer diodes. Charge carrier mobility in these devices matches to state-of-the-art values reported for PVK and PFO polymers in literature. The rectifying behaviour exceeds several orders of magnitude and

is well explained by the Schottky model. In general, transport characteristics of the diodes can be quantitatively modelled by taking a distribution of traps into account and a field dependence of the mobility. These are two typical assumptions for semiconducting polymers, which are justified by the amorphous structure leading to energetically broadened band-tails. As a consequence the field dependence of variable range hopping emerges and a distribution of trap states can be found close to the band edges. Regarding the x-ray sensitivity of these diodes, the reported findings are more complex and in the following an explanation of the observed phenomena is sought. In particular two different regimes of x-ray photocurrent generation have to be distinguished: One regime in which the response is fast and shows a box-like shape, following directly aperture and closure of the x-ray shutter. In the second regime the response is slower and follows a saw-tooth shape but offers an order of magnitude increase in sensitivity. The first regime is associated with reverse bias and follows in its behaviour the standard model for semiconductor based detectors. The second regime instead is observed in thin polymer diodes which are operated in forward regime. As such it is accompanied by a large background current. Here a simple model is proposed to account for the observed findings. The basic mechanism of diode operation and photocurrent generation for both regimes is depicted schematically in Fig. 4.10. When the diode is operated in dark in forward regime, holes can be injected at the MoO₃ layer by the transfer of an electron from the HOMO level into the conduction band MoO₃. Literature describes this process as very favourable due to the low energy of the MoO₃ conduction band and the strong interfacial dipole between Al and MoO₃. Extraction of carriers happens at the Au electrode without additional barriers. As a consequence in this regime current is only limited by traps in the semiconductor and the carrier concentration which builds up according to the SCLC model. When operated in reverse the current is limited by the hole injection from the Au electrode. This is only achieved by an electron transfer from the HOMO level into the Au-Fermi level. Due to Schottky contact formation, this transfer has to happen over a barrier, which suppresses current in reverse operation. When exposed to X-ray, excitons are formed which separate into holes and excess electrons in the semiconductor. When operated in reverse, the electric

field separates the two charges and they are collected at the respective electrodes. The employed organic semiconductors are p-type conductors. Excess electrons become trapped and move at much slower speeds. Therefore effective charge collections happens only from excitons which are generated in vicinity of the gold electrode. In the remaining volume of the semiconductor excitons just recombine. This explains the almost independent (or even decreasing) sensitivity with respect to diode thickness. In conclusion we call this limited charge collection mechanism. In forward operation, a constant SCLC background current and carrier concentration is present in the device. Again excitons dissociate due to the electric field. Now we propose that electrons become trapped in the semiconductor while holes participate as carriers in the diode current. Due to charge neutrality holes enter continuously from the MoO₃ layer to counterbalance the charge of the trapped electrons. Thus as a consequence of x-ray exposure the carrier concentration of the semiconductor is modulated and consequently much larger sensitivity values can be obtained. We term it the conductivity modulation mechanism. For this mechanism the kinetics are limited by the slow annihilation of trapped electrons, which happens at the timescale of seconds. A steady state is reached in this mechanism when the annihilation of trapped excess electrons is as fast as their generation by x-ray. The former process gains in velocity with x-ray exposure due to an increase in hole carrier concentration and in the related probability of hole- trapped electron recombination. After closure of the x-ray shutter, trapped electrons still prevail in the semiconductor until recombination or migration to an electrode happens. This leads to the observed slow return to the background SCLC current level. In conclusion the conductivity modulation mechanism explains the saw-teeth shape of the photocurrent signal and its increase in magnitude. We note however, that this regime is accompanied by a large dark current. For detector operation this could be limiting as in addition to pure sensitivity also the signal to noise ratio is an important figure of merit and it is expected to be reduced in the presence of a large dark-current.

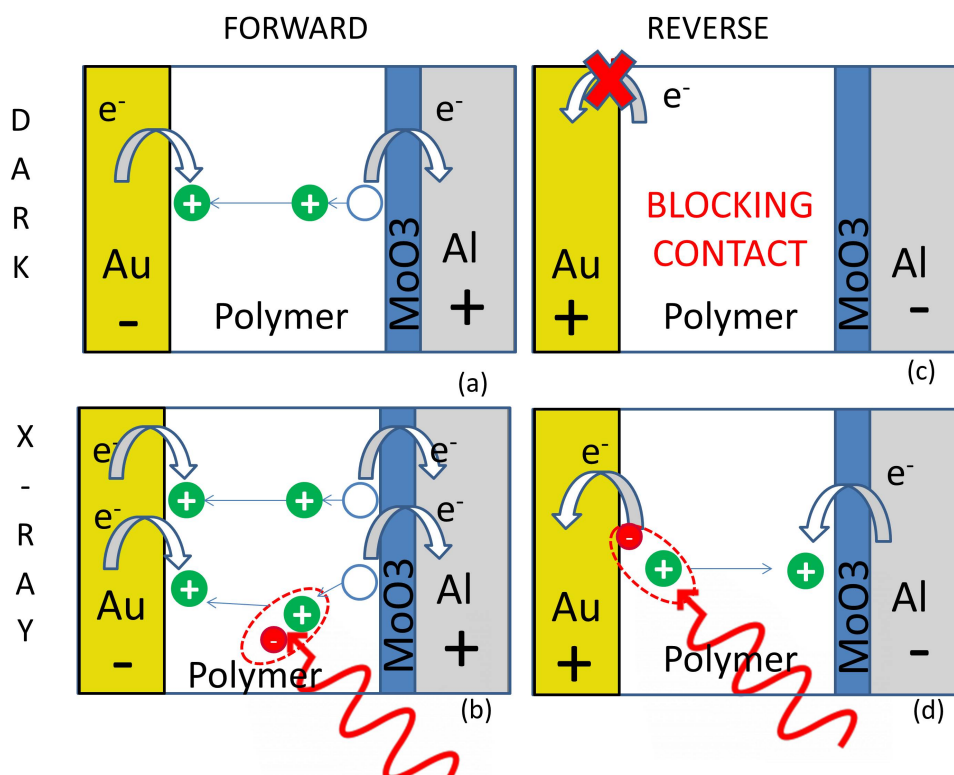


Figure 4.10: Schematic diagram showing the working principles of semiconductor polymer-based x-ray detectors: (a) In forward bias, charge injection happens at MoO₃/Al interface, the diode is conducting. (b) Under x-ray illumination, exciton states are created. Negative charges get trapped at the polymer. For charge neutrality the amount of charge carrier increases, the diode becomes more conductive. (c) In reverse, no charges are injected into the polymer. No current is measured. (d) Under x-ray illumination, excitons dissociate and generated charges are collected at the electrodes.

4.2 NP-polymer blend diodes

Introduction In this chapter diodes are investigated which contain a composite of semiconducting polymer and nanoparticles. Fabrication of these devices follows the procedure used to obtain the pure polymer diodes, instead that the active layer was spin-cast from a solution containing nanoparticles and polymer. Preparation of this solution has turned out to be very critical as agglomerates of nanoparticles are easily formed during mixing. This process was avoided by sonication. In the following we detail first on the

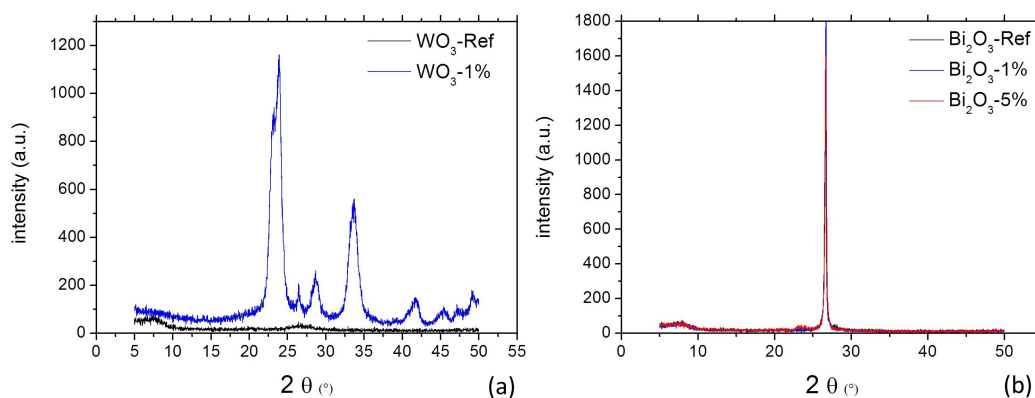


Figure 4.11: The X-ray diffraction (XRD) measurements were performed on drop-cast WO₃ and Bi₂O₃ nanoparticle) films (from toluene). The results are depicted as black lines in Fig. 9(a) and (b). The WO₃ does not exhibit any peak of diffraction, while Bi₂O₃ sample has a intense response at by 27°. When NPs are added to PVK in different concentrations the response of XRD is completely different for WO₃, but remains similar for Bi₂O₃. Interpretation of these findings is unclear at the moment.

morphology of the prepared films using a variety of techniques. In the second subchapter we investigate the electronic properties of the diodes. In the third sub-chapter we finally the report the x-ray detection properties of NP-polymer devices.

4.2.1 Morphological characterization

X-ray diffraction (XRD) measurements were performed on drop-cast WO₃ and Bi₂O₃ nanoparticle films (from toluene). The X-ray diffractograms of samples of differing NP content are presented in Fig. 4.11. The pure NP-toluene solution diffractogram is compared to the XRD response of NP-PVK blends. It is worth noting that a change of the Bi₂O₃ concentration with respect to the polymer does not affect the XRD pattern, which remains always unvaried in its shape for 1 wt%, 5wt% and 100 wt% ratios. In this case the scattering angle can be observed at $2\theta \simeq 27$. On the contrary, the XRD patterns show that crystallinity of the WO₃ nanoparticles changed with varying the NPs amount with respect to polymer. The XRD peak of pure

NP-toluene solution has extremely large full width at half maxima (FWHM) resulting overlap of peaks and hence nanoparticles exhibited XRD amorphous nature. On the other hand as the ratio of NPs changed to 1wt% and 5wt%, the peaks are clearly separated due to increased crystalline nature of WO₃ nanoparticles.

The spectra were compared to those obtained from the nanoparticle powder immediately after its fabrication. They were provided by Nanograde. The scattering pattern for WO₃ nanoparticles shows a more complex behaviour. Interestingly the spectra of the nanoparticle dispersed in the polymer is very similar to the one obtained in pure powder as provided by Nanograde. Instead when the solution is dropcast to leave a pure film of nanoparticles the diffraction peak disappears and a broad amorphous structure results. From these patterns the Scherrer formula was applied to estimate the particle size. For WO₃ a value of 16 nm was obtained whereas Bi₂O₃ resulted in 14 nm.

The X-ray diffraction patterns were also compared with reported standard diffraction patterns of different crystalline types (Verma et al. *Journal of Colloid and Interface Science* 453 (2015) 60–68).

Transmission electron microscopy (TEM) was used to investigate the particle size and their dispersion, the result is shown in Fig. 4.12. WO₃ particles seem to be better dispersed in the polymer than Bi₂O₃ particles. Thanks to the high contrast provided to the conductive copper grid, it possible to assess the size of nanoparticles and the result matches within the measurement uncertainty with the sizes provided by Nanograde: 16 nm for WO₃ and 14 nm for Bi₂O₃. However, especially the Bi₂O₃ particles can be seen in the form of black spots, whose size ranging from 30 to 200 nm. It can be ascribe to formation of NPs agglomerations during the drying procedure to prepared TEM samples.

The distribution of WO₃ nanoparticles in the PVK layer has been examined using the Atomic Force Microscopy (AFM) technique. AFM images for the PVK film blended with 1.25%, 2.5%, 5% and 10% wt of WO₃ nanoparticles are shown in Figure 4.13, respectively. The experiment has been performed in order to evaluate the nanoparticles size, their dispersion and the size of aggregations at the surface of the blend film. It was observed that the increase of the nanoparticle concentration changes the amount of NPs on

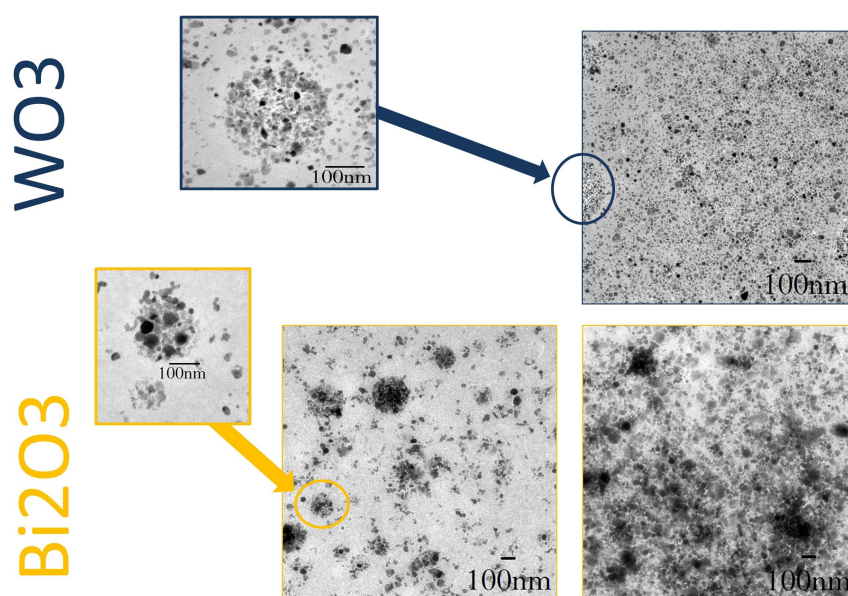


Figure 4.12: The Figure shows TEM images of drop-cast layers containing 10 wt% WO_3 and Bi_2O_3 nanoparticles with respect to PVK. The majority of the nanoparticles have diameters well-within the range of 10-30 nm for which larger particles are attributed to the combination between two or more nanoparticles.

the surface of the blend layer. The comparison between figures 4.13(1) and (2) clearly highlights that the NPs tend to create aggregations and to go up to the surface during the spin-coating process. Despite the spin-coating of the solution was performed immediately after the sonic horn ultrasonication, the formation of cluster is evident. A little variation on the NPs concentration causes a great change in the nanoparticle agglomerations at the surface. That means that during the evaporation of the solvent, the polymer tend to create Van der Waals bonds between its chains, as result, the nanoparticles comes across each other and form agglomerations. The segregation process on the surface is eased due to little size (10-30 nm). On the contrary, bigger Bi_2O_3 NPs (100-300nm) show the inverse behaviour so they deposit

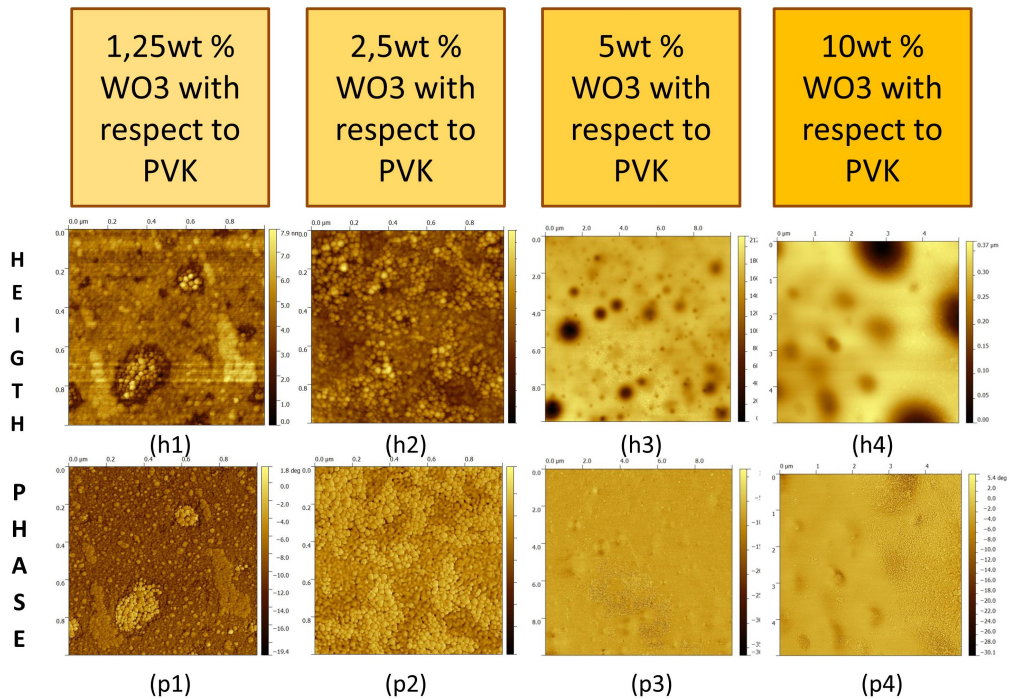


Figure 4.13: AFM topographies and phase maps of PVK polymer films containing increasing amount of WO₃ nanoparticles. The images show increasing roughness and inhomogenities in films with larger nanoparticle content. The finding is attributed to excessive nanoparticle aggregation and changes in viscosity.

on the bottom, as reported by other articles.[?]. The tendency of NPs to agglomerate has been also demonstrated by another structural characterization techniques, SEM. Figure 4.14 show SEM images of PVK containing 8 wt% of WO₃ nanoparticles, obtained after sonication by sonic horn for 30 minutes. Also in this case, inhomogenities and aggregates at the interface are observed. When the concentration of nanoparticle increase over 2.5%wt the quality of the surfaces drastically gets worse, as it is demonstrated by Figures 4.13(h3),(h4) and Figure 4.14. The top surface Al/MoO₃/polymer plays the main role of injection layer, so the observed nanoparticles surface distribution for high concentration may reduce the injected charges and their mobility into the blend layer. Eventually, it could results in a decrease of forward current in diodes.

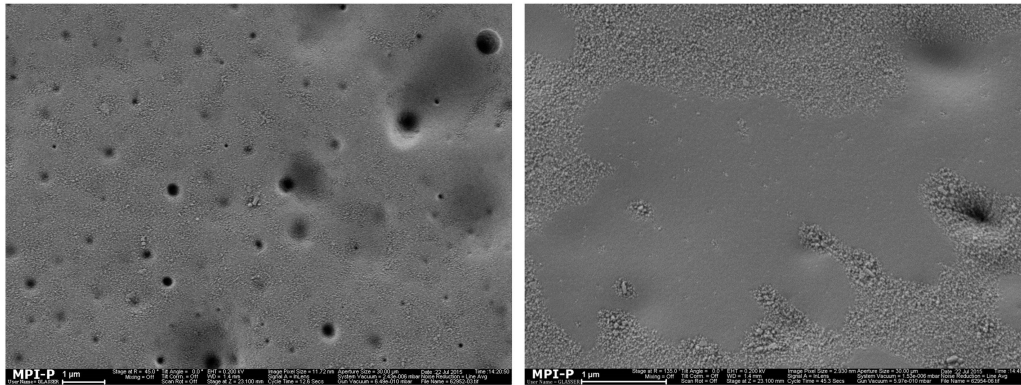


Figure 4.14: SEM images of PVK containing 8 wt% of WO₃ nanoparticles, obtained after sonication by sonic horn for 30 minutes. The figure shows inhomogenities and aggregates at the interface, causing a reduction of mobility and current measured in diodes. The right picture shows strong phase separation due to the tendency of the NPs to aggregate.

4.2.2 Electrical characterization

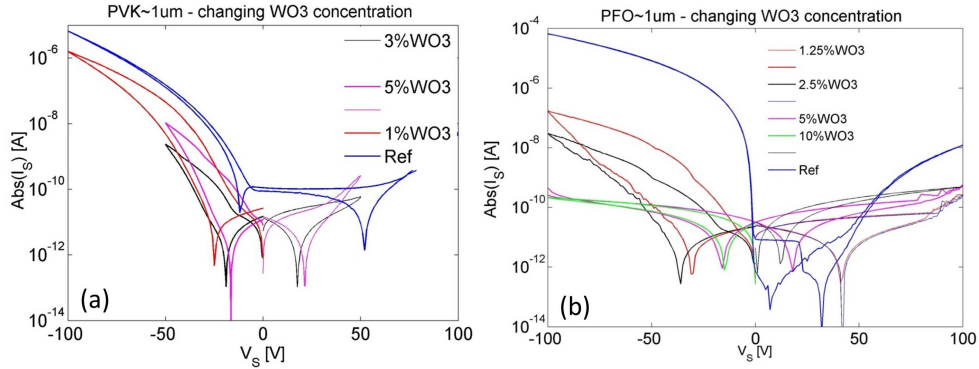


Figure 4.15: Dark current-voltage characteristics nanoparticle polymer composite diodes with varying composition as given in weight% of nanoparticles. The composite layer thickness was kept constant at 1 μm . (a)PVK-based and (b)PFO-based diodes.

IV measurements on diodes in the standard architecture containing polymer-nanoparticle composites were performed as describe in the method section. Fig. 4.15 shows some characteristic measurement for diodes based on PVK and PFO. The nanoparticle content was varied by using differently concentrated polymer nanoparticle solutions for spin coating. Homogeneous films were obtained only for a maximum nanoparticle loading of 5% for WO₃ in PVK and 10% for WO₃ in PFO. As films started to become inhomogeneous at higher nanoparticle loadings for PVK, maximum applied voltages were reduced to prevent diode breakdown. For comparison Fig. 4.15 contains also the reference device containing pure polymer. In general for PVK and PFO a strong reduction in diode current density is noted in combination with the occurrence of hysteresis in the IV scan. Here hysteresis means that in forward direction, the current is larger when the absolute value of the voltage is increasing during the scan. Instead when doing the backward scan with decreasing voltage, a lower current is measured. Both deteriorations of diode properties increase monotonically with NP content. In addition the rectification behaviour deteriorates. At 50V it reduces from 1,5e3 in the pristine PVK device to 4,6e2 in the 1 wt% blend devices and to 18 in 3wt% blend devices. A similar reduction in rectifying factor happens for PFO based de-

vices, which decreases from $2e+5$ for pristine PFO to roughly 1 for 10wt% blend devices. Changes in the rectification ratio are mainly caused by the reduction in forward current. Under reverse current the properties are less affected. This hints to the fact that NP addition impacts on transport in diodes by reducing the mobility of the material. Instead the appearance of hysteresis is explained by the creation of deep trap states due to the presence of NPs. The deep trap states are not filled when the voltage sweep starts and carriers enter the semiconductor. With the proceeding of the scan the states become filled and the current reduces in time. Decreasing the potential again to zero leads to a slow removal of trapped carriers from the diode. We hypothesize that these trap states are directly related to the polar surface of the oxidic nanoparticles which interacts directly with charge carriers. For example a negative surface potential, as typical for oxides, would attract positive hole carriers and trap them.

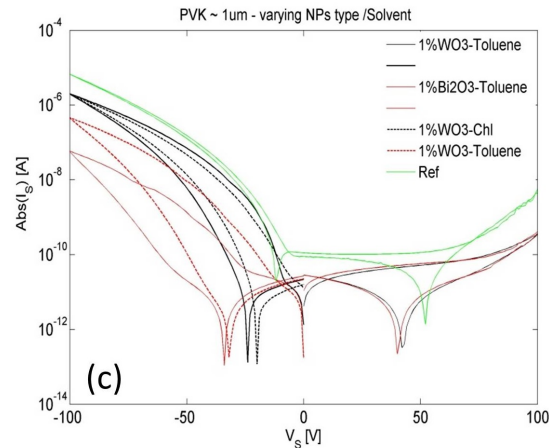


Figure 4.16: Dark current-voltage characteristics nanoparticle PVK composite diodes comparing the impact of WO₃ and Bi₂O₃ nanoparticles. The composite layer thickness was kept constant at 1 μm .

Next we investigated the impact of the Nanoparticle type on diode performance. Fig. 4.16 shows diode IV curves for PVK based diodes containing 1% of WO₃ or Bi₂O₃ NPs. In addition for WO₃ nanoparticles also the spin-casting solvent has been varied to replace toluene by chloroform. In this plot we also show the reference device containing pure polymer. The plot show

that both types of nanoparticles lead to the discussed degradation. However effects caused by Bi₂O₃ nanoparticles are stronger. Instead the solvent has only a small impact in this case and diodes of the same composition show only small variation when the spin coating solvent was changed. This finding seems to be directly related to the morphological characterization. Bi₂O₃ nanoparticles were shown to form larger aggregates in TEM thus they are expected to disturb ordered polymer domains with good charge transporting properties in a stronger way.

4.2.3 X-ray detector properties

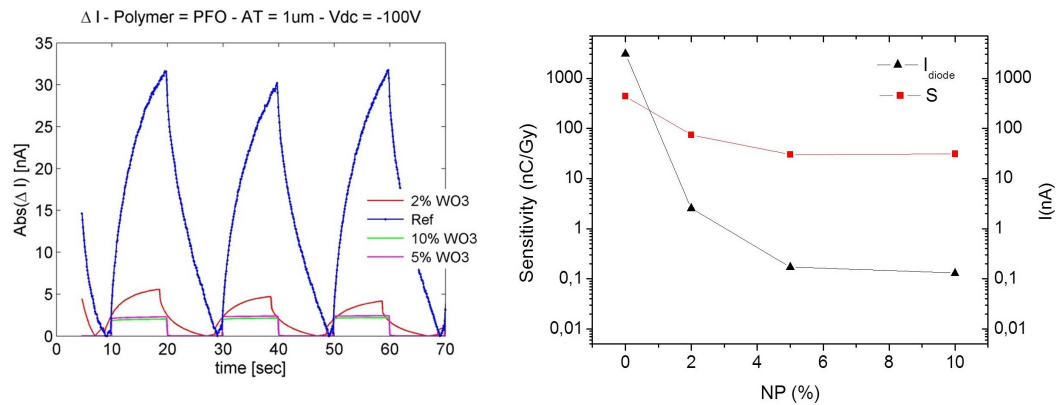


Figure 4.17: Impact of nanoparticles on diode detector properties in forward bias: (a) X-ray photocurrent as a function of time in PFO diodes containing various amounts of WO₃ nanoparticles. The X-ray shutter was opened for 10 s at $t=10$ s, 30s and 50s. (b) X-ray sensitivity and dark current as a function of NP content.

In analogy to the previous chapter we compare the photoresponse of the polymer NP composite diodes. Again a voltage of ± 100 V was applied to the gold electrode while the aluminium electrode was grounded. The resulting current was continuously monitored. At specific time intervals the shutter of a Mo X-ray tube was opened for 10 sec. The experiment was repeated at least 3 times to probe the stability of the measured response. Characteristic X-ray responses for PFO based diodes operated in forward regime are shown

in Fig. 4.17a. In this experiment the content of WO₃ nanoparticles was continuously increased to reach an upper value of 10% as given by the stability of the film (see morphological analysis). The increase in nanoparticle content leads to a significant variation of the shape of the photoresponse. Initially the saw-tooth shape was observed as discussed in the previous chapter. Adding 2% of NP reduces the magnitude of the response. In addition a transition into the regime with the box-like response can be observed. At nanoparticle contents exceeding 2% only a smaller but immediate response to x-ray, identical to the behaviour under reverse bias is observed. By varying the dose-rate of the radiation we determine the sensitivity of the polymer-nanoparticle diodes. All devices obey a linear relationship between photoresponse and dose rate. The resulting values for S are plotted in Fig. 4.17b as a function of NP concentration. A monotonic reduction in sensitivity with increasing nanoparticle concentration is observed. At 10% nanoparticles, the sensitivity is reduced by a factor of 30 with respect to the pure polymer diode. Thus although X-ray absorption increases due to the addition of the high-Z compound, no increase in the amount of charge collected at the electrodes can be observed in this regime. However, the addition of nanoparticles improve the dark-current properties of the diode detectors. Without nanoparticles the dark current exceeds 1 μA . Addition of nanoparticles reduces this value by orders of magnitude to reach a value of 100 pA at 10% loading. This improvement will impact on the signal to noise properties of the detector.

In reverse operation of diodes a different impact of nanoparticles is observed. In Fig. 4.18a shows the photocurrent as a function of time as recorded while the X-ray shutter was opened and closed for three intervals of exposure of 10 s duration. As tested diodes we use as reference the pure PFO polymer diode while the other diodes contain WO₃ nanoparticles up to a maximum concentration of 10%. For all cases a fast, box-like response as discussed in the previous chapter is observed. Thus we conclude that all diodes follow the charge collection mechanism. Varying the dose rate allows to plot the photoresponse as a function of dose rate as shown in Fig. 4.18b. For all NP concentrations a linear response is obtained allowing to quantify their X-ray sensitivity. The resulting values are plotted in Fig. 4.18b as a function of NP concentration in combination with the dark-current of the devices. An

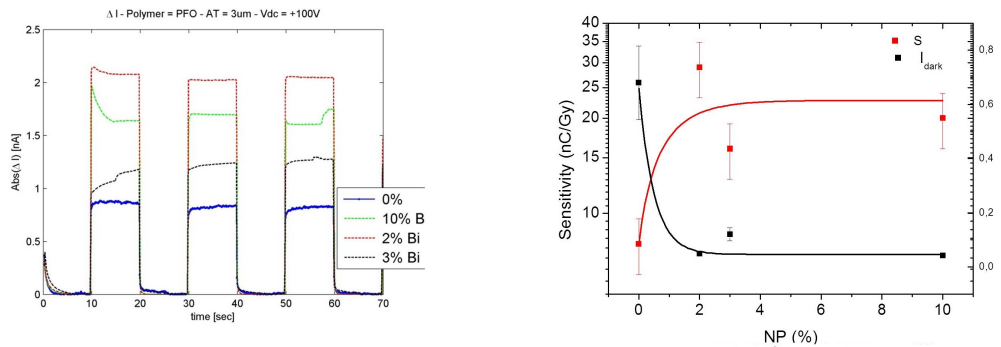


Figure 4.18: Impact of NPs on diode detector properties in reverse bias: (a) X-ray photocurrent as a function of time in PFO-diode containing various amount of WO_3 nanoparticles. (b) Plot of the photoresponse as a function of x-ray dose rate to extract x-ray sensitivities. (c) sensitivity and dark current as a function of NP content. The lines are guide to the eyes.

increase in sensitivity is observed by the addition of nanoparticles up to 2%. At higher concentrations, no further improvement is observed. Instead the response seem to be even reduced although a statistically significant analysis would require more data points. The dark-current is also improved due to the nanoparticle addition reaching a value of less than 100 pA.

4.2.4 Discussion and conclusion

The performed experiments allow to draw several conclusions about the improvement of polymer diode X-ray detectors due to the addition of nanoparticles: First the technical difficulty of preparing homogene nanoparticle polymer composite films has to be stressed. As the morphological investigation has demonstrated aggregation of nanoparticles sets in already at low nanoparticle concentration. In addition viscosity and surface tension of the composite film vary with nanoparticle content making spin coating difficult. In particular larger defects and phase separation start to appear at the surface of the polymer composite at concentrations exceeding 8% for WO_3 nanoparticles. For Bi_2O_3 nanoparticles even stronger artifacts were observed. Second, the addition of nanoparticles has also a strong impact on the electrical properties of the polymer diodes. Deterioration of diode current in forward direction, appearance of hysteresis were observed. As a consequence the rectification

behaviour of the diodes reduced and instabilities in current occur. For Bi₂O₃ nanoparticles the effects were pronounced hinting to a connection to their stronger impact on composite morphology. In general a minimization of nanoparticle size and dispersion must be the main goal to reduce the deterioration of electrical properties. In addition also the surface functionalization of nanoparticles has to be investigated in more detail. We hypothesize that polar or even charge surface groups of the oxide surface are responsible for the formation of trap states in the semiconductor and related hysteresis. Third, the impact on x-ray detection properties depends on the regime of diode operation. Here a detailed picture emerges from the study: In forward regime x-ray detection with high sensitivity occurs via the modulation of the diode conductivity by x-ray generated charge carriers. Detection in this regime relies on fast moving carriers as the generated photocurrent density results as the product of generated carriers \times mobility \times electric field. Reducing the mobility due to the incorporation of Nanoparticles has a strongly deteriorating effect on the conductivity modulation which cannot be compensated by the increase in x-ray absorption. Once the carrier mobility is below a certain limit, only excitons which dissociate in direct vicinity of the gold electrode can be dissociated and their charge gets collected. In the reverse regime, high Z-nanoparticles allow to improve polymer diode detectors, although the mobility gets reduced. The reason is that the limit for charge collection in pure polymer diodes is given by the electron mobility, which is already in the pure material low and results in charge collection only from excitons generated close to the gold electrode (see 4.1). Addition of nanoparticles reduces hole mobility but seems to have a low impact on electron mobility. Instead it increases x-ray absorption and hence an increase in sensitivity is observed. For PFO the increase amounts to a factor of five. In addition a reduction of dark current is noted. This could be attributed to a general reduction in dark current or to an interfacial process probably related to the agglomeration of nanoparticles at one of the interfaces.

Chapter 5

Conclusions

Conjugated polymers are promising candidate for radiation detection exploiting their unique electrical conductivity and photonic properties. They can be tailored with sensitivity to various particles, such as low energy electrons, protons, α -particles, β -rays, X-rays and γ -rays. Conjugated polymers have a low atomic number, similar to human tissue, as they have similar elemental compositions. As a result, they have comparable stopping power and absorption coefficient for radiation particles. This similarity can be exploited for medical applications, as radiation dosimetry detectors. To result in optimized X-ray detection properties, polymer diodes must be designed to achieve (i) high hole as well as electron mobility to maximize charge collection, (ii) high rectifying behaviour to achieve a low dark current and a strong signal to noise ratio and (iii) a controlled stopping power which results in low x-ray absorption when detectors should be applied to medical dosimetry or maximized X-ray detection for application in X-ray imaging and spectrometry. Polymer diodes which combine these properties are still elusive and the scope of this thesis is to improve on the materials and operation mechanism of polymer diodes for X-ray detection.

To this aim polymer diodes based on two different semiconducting polymers, polyvinylcarbazole (PVK) and poly(9,9-dioctyluorene) (PFO) have been fabricated during a 4 month stay at the Max-Planck Institute for Polymer Research, Mainz, Germany. Optimized rectifying behaviour was obtained by using a gold electrode for hole extraction combined with a MoO₃

modified Aluminum electrode for hole injection in forward operation and electrode extraction. In order to control the X-ray stopping power, high-Z nanoparticle Bi₂O₃ or WO₃ were added to realize a polymer-nanoparticle composite with optimized properties. Careful characterization of morphologic properties by AFM, SEM, TEM and XRD gave crucial information about nanoparticle distribution and agglomeration in the composite. It was found that only low nanoparticle contents below 8% resulted in sufficiently homogeneous films for reliable diode operation. Further the transport mechanism of the diodes was studied by modelling of the IV- characteristics for diodes of varying thickness. The ideal theory for a space-charge limited current (SCLC) was not applicable and had to be extended to account for a distribution of trap states and a field dependent mobility. As high field mobilities values of 1.3×10^{-5} cm²/Vs and 5×10^{-7} cm²/Vs were obtained for PFO and PVK respectively which compare to literature findings.

X-ray detection properties of the diodes was performed at the Physics Department of the University of Bologna. The set of tested diodes contained device which varying thickness, polymer composition and nanoparticle content. X-ray induced photocurrents were characterized in forward as well as reverse operation of diodes. In addition the x-ray sensitivity of the device was determined by varying the x-ray dose rates. From these experiments the following conclusions can be drawn:

a) The fabricated polymer diodes worked as direct X-ray detectors with state of the art sensitivity reaching 14 $\mu\text{C}/\text{Gy}/\text{cm}^2$ when operated in reverse. b) Moreover, the devices offer photo-detection in two different operation regimes. One providing a fast, box-shaped response with state of the art sensitivity. The other following a slower kinetics but providing a sensitivity which is two orders of magnitude higher. c) A model was proposed to interpret the two regimes: The first regime based on the extraction of photogenerated carriers, the second based on the modulation of conductivity by photogenerated carriers. d) Nanoparticles can improve X-ray sensitivity by almost an order of magnitude when devices are operated in reverse (box-shaped photocurrent). In contrast they disturb the photocurrent generated in forward operation. e) Incorporation of higher content of nanoparticles (exceeding 8%) is hard to achieve without a significant disturbance of the

homogeneity of the film.

Bibliography

- [1] Hans-Günther Moser. Silicon detector systems in high energy physics. *Progress in Particle and Nuclear Physics*, 63(1):186 – 237, 2009.
- [2] F Nava, G Bertuccio, A Cavallini, and E Vittone. Silicon carbide and its use as a radiation detector material. *Measurement Science and Technology*, 19(10):102001, 2008.
- [3] G. Harding and B. Schreiber. Coherent x-ray scatter imaging and its applications in biomedical science and industry. *Radiation Physics and Chemistry*, 56(1–2):229 – 245, 1999.
- [4] Haizheng Zhong, YongSheng Zhao, Yongfang Li, and Qibing Pei. Photoluminescence quenching of conjugated polymer nanocomposites for gamma ray detection. *Nanotechnology*, 19(50):505503, 2008.
- [5] Christopher R. Newman, Henning Sirringhaus, James C. Blakesley, and Robert Speller. Stability of polymeric thin film transistors for x-ray imaging applications. *Applied Physics Letters*, 91(14):–, 2007.
- [6] Ravindra Yaparpalvi, Doracy P. Fontenla, and Bhadrasain Vikram. Clinical experience with routine diode dosimetry for electron beam radiotherapy. *International Journal of Radiation Oncology*Biography*Physics*, 48(4):1259 – 1265, 2000.
- [7] N. Uhlmann, M. Salamon, F. Sukowski, and V. Volland. Characterization and comparison of direct and indirect converting x-ray detectors for non-destructive testing (ndt) in low-energy and high-resolution applications. *Nuclear Instruments and Methods in Physics Research Section*

- A: Accelerators, Spectrometers, Detectors and Associated Equipment*, 591(1):46 – 49, 2008. Radiation Imaging Detectors 2007 Proceedings of the 9th International Workshop on Radiation Imaging Detectors.
- [8] Michael Moll. Radiation tolerant semiconductor sensors for tracking detectors. *Nuclear Instruments and Methods in Physics Research Section A: Accelerators, Spectrometers, Detectors and Associated Equipment*, 565(1):202 – 211, 2006. Proceedings of the International Workshop on Semiconductor Pixel Detectors for Particles and Imaging PIXEL 2005 International Workshop on Semiconductor Pixel Detectors for Particles and Imaging.
- [9] C. Jacoboni, C. Canali, G. Ottaviani, and A. Alberigi Quaranta. A review of some charge transport properties of silicon. *Solid-State Electronics*, 20(2):77 – 89, 1977.
- [10] † Yasuhiko Shirota*, , and Hiroshi Kageyama‡. Charge carrier transporting molecular materials and their applications in devices. *Chemical Reviews*, 107(4):953–1010, 2007. PMID: 17428022.
- [11] Alex C. Mayer, Shawn R. Scully, Brian E. Hardin, Michael W. Rowell, and Michael D. McGehee. Polymer-based solar cells. *Materials Today*, 10(11):28 – 33, 2007.
- [12] Jiri Janata. Organic semiconductors in molecular electronics. *Phys. Chem. Chem. Phys.*, 5:5155–5158, 2003.
- [13] Kyu Won Lee, Kyu Hyun Mo, Jae Won Jang, and Cheol Eui Lee. Proton-irradiation effect on the luminescence of the meh–ppv conjugated polymer. *Solid State Communications*, 141(2):57 – 60, 2007.
- [14] J.C. Blakesley, P.E. Keivanidis, M. Campoy-Quiles, C.R. Newman, Y. Jin, R. Speller, H. Sirringhaus, N.C. Greenham, J. Nelson, and P. Stavrinou. Organic semiconductor devices for x-ray imaging. *Nuclear Instruments and Methods in Physics Research Section A: Accelerators, Spectrometers, Detectors and Associated Equipment*, 580(1):774 – 777, 2007. Proceedings of the 10 th International Symposium on Radiation Physics ISRP 10.

- [15] Katsumi Yoshino, Shigenori Hayashi, and Yoshio Inuishi. Effects of electron irradiation on electrical conductivity of polyacetylene. *Japanese Journal of Applied Physics*, 21(9A):L569, 1982.
- [16] Christopher A. Mills, Akarin Intaniwet, Maxim Shkunov, Joseph L. Keddie, and Paul J. Sellin. Flexible radiation dosimeters incorporating semi-conducting polymer thick films, 2009.
- [17]
- [18] C. Karnutsch, C. Pflumm, G. Heliotis, J. C. deMello, D. D. C. Bradley, J. Wang, T. Weimann, V. Haug, C. Gärtner, and U. Lemmer. Improved organic semiconductor lasers based on a mixed-order distributed feedback resonator design. *Applied Physics Letters*, 90(13):–, 2007.
- [19] L.C. Poças, K.R. Campos, S.L. Nogueira, E. Piovesan, R.A. Silva, M.L. Vega, and Alexandre Marletta. Absorption and emission properties of {LBL} {PPV} films deposited on {ITO} electrodes. *Journal of Non-Crystalline Solids*, 354(42–44):4852 – 4855, 2008. Glass and Related Materials 8Proceedings of the 8th Brazilian Symposium on Glass and Related Materials and 4th International Symposium on Non-Crystalline Solids8th Brazilian Symposium on Glass and Related Materials and 4th International Symposium on Non-Crystalline Solids.
- [20] Claudio Giroto, Barry P. Rand, Jan Genoe, and Paul Heremans. Exploring spray coating as a deposition technique for the fabrication of solution-processed solar cells. *Solar Energy Materials and Solar Cells*, 93(4):454 – 458, 2009. Processing and Preparation of Polymer and Organic Solar Cells.
- [21] Frederik C. Krebs. Fabrication and processing of polymer solar cells: A review of printing and coating techniques. *Solar Energy Materials and Solar Cells*, 93(4):394 – 412, 2009. Processing and Preparation of Polymer and Organic Solar Cells.
- [22] C. Zhang, H. von Seggern, K. Pakbaz, B. Kraabel, H.-W. Schmidt, and A.J. Heeger. Blue electroluminescent diodes utilizing blends of poly(p-

- phenylphenylene vinylene) in poly(9-vinylcarbazole). *Synthetic Metals*, 62(1):35 – 40, 1994.
- [23] G. Knoll. *Radiation Detection and Measurement*. John Wiley & Sons, Ltd, 4th ed 2011.
- [24] H. Kempa M. Hambsch K. Reuter M. Stanel G. C. Schmidt, M. Bellmann and A. C. Hübner. Mrs online proc. libr., 2011,1285.
- [25] S O Kasap. X-ray sensitivity of photoconductors: application to stabilized a-se. *Journal of Physics D: Applied Physics*, 33(21):2853, 2000.
- [26] B.G. Streetman and S. Banerjee. *Solid state electronic devices*. Prentice-Hall Upper Saddle River, NJ, 6th edition, 2006.
- [27] Daniele Braga, Marcello Campione, Alessandro Borghesi, and Gilles Horowitz. Organic metal-semiconductor field-effect transistor (omesfet) fabricated on a rubrene single crystal. *Advanced Materials*, 22(3):424–428, 2010.
- [28] Jungmin Kwon, Y. G. Seol, Nae-Eung Lee, and IlSub Chung. Study on ohmic contact improvement of organic schottky diode utilizing self-assembled monolayer and pedot:pss layers. *Journal of Vacuum Science & Technology A*, 28(4), 2010.
- [29] Zhaoyue Lü, Zhenbo Deng, Jianjie Zheng, Ye Zou, Zheng Chen, Denghui Xu, and Yongsheng Wang. Ohmic contact and space-charge-limited current in molybdenum oxide modified devices. *Physica E: Low-dimensional Systems and Nanostructures*, 41(10):1806 – 1809, 2009.
- [30] P. de Bruyn, D.J.D. Moet, and P.W.M. Blom. All-solution processed polymer light-emitting diodes with air stable metal-oxide electrodes. *Organic Electronics*, 13(6):1023 – 1030, 2012.
- [31] P. de Bruyn, A. H. P. van Rest, G. A. H. Wetzelaer, D. M. de Leeuw, and P. W. M. Blom. Diffusion-limited current in organic metal-insulator-metal diodes. *Phys. Rev. Lett.*, 111:186801, Oct 2013.
- [32] Gurney RW Mott NF. *Electronic processes in ionic crystals*, 1940.

- [33] M. Meier, S. Karg, and W. Riess. Light-emitting diodes based on poly-p-phenylene-vinylene: Ii. impedance spectroscopy. *Journal of Applied Physics*, 82(4), 1997.
- [34] S.A. Moiz, M.M. Ahmed, Kh.S. Karimov, F. Rehman, and J.-H. Lee. Space charge limited current–voltage characteristics of organic semiconductor diode fabricated at various gravity conditions. *Synthetic Metals*, 159(13):1336 – 1339, 2009.
- [35] P N Murgatroyd. Theory of space-charge-limited current enhanced by frenkel effect. *Journal of Physics D: Applied Physics*, 3(2):151, 1970.
- [36] A. Rouis, C. Dridi, I. Dumazet-Bonnamour, J. Davenas, and H. Ben Ouada. Transport mechanism and trap distribution in ito/azocalix[4]arene derivative/al diode structure. *Physica B: Condensed Matter*, 399(2):109 – 115, 2007.
- [37] Peter Mark and Wolfgang Helfrich. Space charge limited currents in organic crystals. *Journal of Applied Physics*, 33(1), 1962.
- [38] Paul Blom and M. Jong. Device physics of polymer light emitting diodes. *Polymers for Advanced Technologies*, 9(7):390–401, 1998.
- [39] Elisabetta Collini and Gregory D. Scholes. Coherent intrachain energy migration in a conjugated polymer at room temperature. *Science*, 323(5912):369–373, 2009.
- [40] P D Townsend, C M Pereira, D D C Bradley, M E Horton, and R H Friend. Increase in chain conjugation length in highly oriented durham-route polyacetylene. *Journal of Physics C: Solid State Physics*, 18(11):L283, 1985.
- [41] Bredas JL Silbey R. Chance RR, Boudreaux OS. *Handbook of Conducting Polymers*. Oxford University Press, Skotheim TA, Ed., Vol. 2, chapter 24, Marcel Dekker, 1986.
- [42] Benjamin J Schwartz, Thuc-Quyen Nguyen, Junjun Wu, and Sarah H Tolbert. Interchain and intrachain exciton transport in conjugated

- polymers: ultrafast studies of energy migration in aligned mehpv/mesoporous silica composites. *Synthetic Metals*, 116(1–3):35 – 40, 2001.
- [43] M. C. J. M. Vissenberg and M. Matters. Theory of the field-effect mobility in amorphous organic transistors. *Phys. Rev. B*, 57:12964–12967, May 1998.
- [44] Pei Yuin Keng, Inbo Shim, Bryan D. Korth, Jack F. Douglas, and Jeffrey Pyun. Synthesis and self-assembly of polymer-coated ferromagnetic nanoparticles. *ACS Nano*, 1(4):279–292, 2007.
- [45] Alexander Pope. *Alexander Pope*. Oxford University Press, USA, 1993.
- [46] K D’Almeida, JC Bernede, F Ragot, A Godoy, FR Diaz, and S Lefrant. Carbazole-based electroluminescent devices obtained by vacuum evaporation. *Journal of applied polymer science*, 82(8):2042–2055, 2001.
- [47] Yi-Sheng Lai, Chia-Hsun Tu, Dim-Lee Kwong, and Jen-Sue Chen. Bistable resistance switching of poly (n-vinylcarbazole) films for non-volatile memory applications. *Applied Physics Letters*, 87(12):122101, 2005.
- [48] HT Nicolai, GAH Wetzelaer, M Kuik, AJ Kronemeijer, B De Boer, and PWM Blom. Space-charge-limited hole current in poly (9, 9-dioctylfluorene) diodes. *Applied Physics Letters*, 96(17):172107, 2010.
- [49] A Intaniwet, CA Mills, M Shkunov, PJ Sellin, and JL Keddie. Heavy metallic oxide nanoparticles for enhanced sensitivity in semiconducting polymer x-ray detectors. *Nanotechnology*, 23(23):235502, 2012.
- [50] Peter Eaton and Paul West. *Atomic force microscopy*. Oxford Univ. Press, 2010.
- [51] Joseph Goldstein, Dale E Newbury, Patrick Echlin, David C Joy, Alton D Romig Jr, Charles E Lyman, Charles Fiori, and Eric Lifshin. *Scanning electron microscopy and X-ray microanalysis: a text for biologists, materials scientists, and geologists*. Springer Science & Business Media, 2012.

- [52] Fabrizio Torricelli, Dario Zappa, and Luigi Colalongo. Space-charge-limited current in organic light emitting diodes. *Applied Physics Letters*, 96(11):113304, 2010.